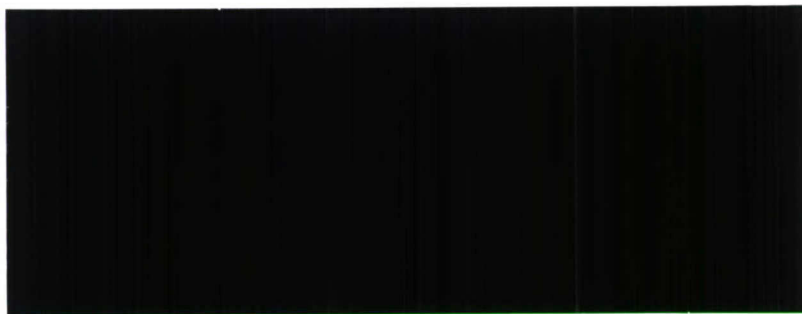


TNO Report



TNO | Knowledge for business



20081027310



Oude Waalsdorperweg 63
P.O. Box 96864
2509 JG The Hague
The Netherlands

www.tno.nl

T +31 70 374 00 00
F +31 70 328 09 61
info-DenV@tno.nl

TNO report

TNO-DV 2008 A325

**Multi-band Frequency Selective Surfaces:
Analysis**

| | |
|-----------------------|--|
| Date | August 2008 |
| Author(s) | A. Francavilla, MSc Dr S. Monni Dr D. Bekers Dr A. Neto Dr G. Gerini N. Fiscante, MSc |
| Classification report | Ongerubriceerd |
| Classified by | drs. W. Pelt |
| Classification date | 1 August 2008 |
| Title | Ongerubriceerd |
| Managementuittreksel | Ongerubriceerd |
| Abstract | Ongerubriceerd |
| Report text | Ongerubriceerd |
| Copy no | 18 |
| No. of copies | 28 |
| Number of pages | 39 (incl. appendices, excl. RDP & distribution list) |

The classification designation Ongerubriceerd is equivalent to Unclassified, Stg. Confidentieel is equivalent to Confidential and Stg. Geheim is equivalent to Secret.

All rights reserved. No part of this report may be reproduced in any form by print, photoprint, microfilm or any other means without the previous written permission from TNO.

All information which is classified according to Dutch regulations shall be treated by the recipient in the same way as classified information of corresponding value in his own country. No part of this information will be disclosed to any third party.

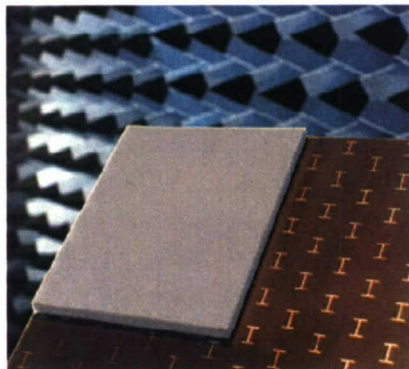
In case this report was drafted on instructions from the Ministry of Defence the rights and obligations of the principal and TNO are subject to the standard conditions for research and development instructions, established by the Ministry of Defence and TNO, if these conditions are declared applicable, or the relevant agreement concluded between the contracting parties.

© 2008 TNO

AQ F09-01-00275

Multi-band Frequency Selective Surfaces: Analysis

De toenemende hoeveelheid van sensoren en communicatiesystemen aan boord van een schip gecombineerd met de wens om deze systemen te integreren in een geïntegreerde mast module resulteert in de uitdaging om meerdere functionaliteiten te integreren in een antenne. Kunnen multi-band frequentie selectieve oppervlakken hiervoor een oplossing bieden?



Probleemstelling

Een huidige trend in ontwikkeling van antennes is de integratie van verscheidene functies in verschillende frequentiebanden die op hetzelfde antenna oppervlak zijn geïmplementeerd. Hiervoor zijn ook nieuwe concepten voor Frequentie Selectieve Oppervlakten (FSS) nodig. Deze structuren moeten doorlatende banden hebben in de frequenties waar de antenne opereert, gescheiden door scherpe stopbanden. Typische toepassingen voor zulke FSSs in combinatie met een antenne zijn het bereiken van goede EM isolatie en een lage radar cross sectie (RCS).

In de afgelopen jaren is in het kader van activiteiten rond FSS bij TNO Defensie en Veiligheid een geavanceerde software tool

ontwikkeld voor de analyse van FSS structuren met meer dan één laag. De tool is ook met succes gebruikt voor het ontwerp van een aantal FSS structuren met verschillende operationele eisen voor verschillende toepassingen. Om multi-band gedrag te kunnen bereiken, moeten FSS structuren met complexe geometrie ontworpen worden.

Beschrijving van de werkzaamheden

Er zijn nieuwe features in de software tool aangebracht om de behandeling van een complexe geometrie en daarmee multi-band gedrag mogelijk te maken. De software tool is uitgerust met een driehoekig mesh en dienovereenkomstig zijn de elektrische en magnetische stromen aan de FSS elementen met Rao Wilton Glisson functies beschreven.

In de afgelopen jaren zijn verschillende optimalisatie technieken voor FSSs in de software geïmplementeerd. Een van deze technieken, bitmapping, heeft als basis element een gehele gemetalliseerde unit cell. Om deze techniek te kunnen toepassen, moet de continuïteit van de stroom tussen naburige unit cellen kunnen worden

gegarandeerd. De bijhorende aanpassingen zijn inmiddels ook in de software tool geïmplementeerd.

De aanpassingen in de software tool zijn gevalideerd door een aantal FSS structuren te analyseren en de resultaten te vergelijken met resultaten in de literatuur.

Resultaten en conclusies

De software tool voor analyse van FSS structuren is uitgebreid en geschikt om FSS structuren te analyseren met een complexe geometrie waarmee multi-band gedrag bereikt kan worden.

De nieuwe ontwikkelingen zijn succesvol getest aan de hand van resultaten beschikbaar in de literatuur.

Het ontwerp van een multiband FSS structuur is beschreven.

Toepasbaarheid

FSS structuren waarmee multi-band gedrag bereikt kan worden, kunnen in combinatie met een antenne gebruikt worden om één front-end te maken waarmee meerdere functionaliteiten tegelijkertijd gerealiseerd kunnen worden. Deze technologie ondersteunt de wens om een groeiend aantal functionaliteiten te integreren in een

geïntegreerde mast module. Tevens kunnen multi-band FSS structuren toegepast worden als radome materiaal wanneer een radome een aantal systemen opererend op verschillende frequentiebanden moet omvatten.

| PROGRAMMA | PROJECT |
|---|--|
| Programmabegeleider ing. L.F. Galle, DMO/DWS&B/RZS&B/OBI | Projectbegeleider drs. W. Pelt, DMO/DWS&B/RZS&B/OBI |
| Programmaleider ir. Y.Rieter-Barrell, Waarnemingsystemen | Projectleider dr. ir. S. Monni, Waarnemingsystemen |
| Programmatitel Integrated Technology Mast Systems | Projecttitel Multi-band Frequency Selective Surfaces |
| Programmanummer V704 | Projectnummer 032.11237 |
| Programmaplanning Start 01-01-2007 Gereed 31-12-2010 | Projectplanning Start 01-01-2007 Gereed 31-12-2008 |
| Frequentie van overleg Met de programma/project- begeleider werd een aantal maal gesproken over de invulling en de voortgang van het onderzoek. | Projectteam ir. A. Francavilla, dr. ir. S. Monni, dr. ir. D. Bekers, dr. ir. A. Neto, dr. ir. G. Gerini and ir. N. Fiscante |

Contact en rapportinformatie

Oude Waalsdorperweg 63
Postbus 96864
2509 JG Den Haag

T +31 70 374 00 00
F +31 70 328 09 61

info-DenV@tno.nl

TNO-rapportnummer
TNO-DV 2008 A325

Opdrachtnummer
-

Datum
augustus 2008

Auteur(s)
ir. A. Francavilla
dr. ir. S. Monni
dr. ir. D. Bekers
dr. ir. A. Neto
dr. ir. G. Gerini
ir. N. Fiscante

Rubricering rapport
Ongerubriceerd

Summary

Present trends in antenna development go toward the integration on the same antenna aperture of more functions operating in separate frequency bands. In view of this, the necessity to look at new Frequency Selective Surface (FSS) concepts becomes evident. These structures should have pass-bands corresponding to the antenna operational frequencies sandwiched between sharp stop-bands. Such FSSs could then be used to obtain good EM isolation and RCS reduction. In the framework of the FSS activities in the last years, TNO Defence, Security and Safety has developed an advanced tool for the analysis of multi-layer FSSs. The tool has also proved to be very suitable for the synthesis of such structures. In particular, it has been applied to the design, manufacturing and testing of several FSSs operating in different single bands and with different operational requirements.

In the frame of Phase I of the Multiband Frequency Selective Surface project defined within the ITM programme, the tool has been upgraded with new features to render it more flexible in handling new complex geometries, necessary to satisfy the new very demanding requirements of multi-band FSSs. In particular, the tool has been equipped with a triangular mesh and correspondingly the electric and magnetic currents on the FSS elements have been discretised in terms of Rao Wilton Glisson functions. Moreover, the application of the bitmapping design technique requires considering completely metallised unit cells and therefore ensuring the continuity of the currents across adjacent cells. A further upgrade in this direction has been introduced in the tool. The new implementations have been tested against results available in the open literature and the obtained agreement is very good.

Contents

| | | |
|----------|---|-----------|
| | Managementuittreksel | 2 |
| | Summary | 4 |
| | Abbreviations | 6 |
| 1 | Introduction | 7 |
| 2 | Application of Multi-band FSSs | 9 |
| 3 | Upgrades to the IEMEN analysis technique | 20 |
| 4 | Conclusions and Recommendations | 36 |
| 5 | References | 37 |
| 6 | Signature | 39 |

Abbreviations

| | |
|-------|---|
| AMC | Artificial Magnetic Conductor |
| FDTD | Finite-Difference-Time-Domain |
| FSS | Frequency Selective Surface |
| IEMEN | Multimode Equivalent Network approach based on the Integral Equation formulation |
| ITM | Integrated Technology Mast |
| LAN | Local Area Network |
| MoM | Method of Moments |
| RWG | Rao Wilton Glisson |

1 Introduction

The number of sensors and communication systems to be allocated in military platforms (e.g. mast of a navy ship, fuselage of an aircraft, top of a land vehicle) is increasingly growing and with it also the number of corresponding antenna systems. However, space, weight and antenna sighting are precious and limited resources in these platforms. Sharing different functionalities on the same antenna aperture to reduce the total number of antennas is therefore highly desirable. The design of such an antenna poses some serious issues in terms of isolation between channels and control of intermodulation products between signals from the simultaneously operating antenna systems. To deal with these issues, the antenna architecture becomes more complex in terms of number of channels in the TR modules and beamforming network. This is why shared aperture antenna technology is still a hot research topic. For example, in [1] the development of a shared aperture array antenna based on wideband double beam technology is described. The FSS designed for such an antenna should have two sharply separated pass-bands. Single band FSSs can also be used as selective ground planes for the design of FSS-integrated multi-band antennas systems. For example, currently U.S.A. Navy ships receive meteorological and oceanographic satellite data in S- and L-band, but starting from 2010, when the new National Polar-orbiting Operational Environmental Satellite System (NPOESS), which is transmitting in X-band, will be launched, the terminals on the ships will have to be upgraded in order to be able to receive also these data. A prototype of multi-band antenna system to cope with this problem is described in [2]. It consists of three nested flat plate array antennas as shown in Fig. 1.1.

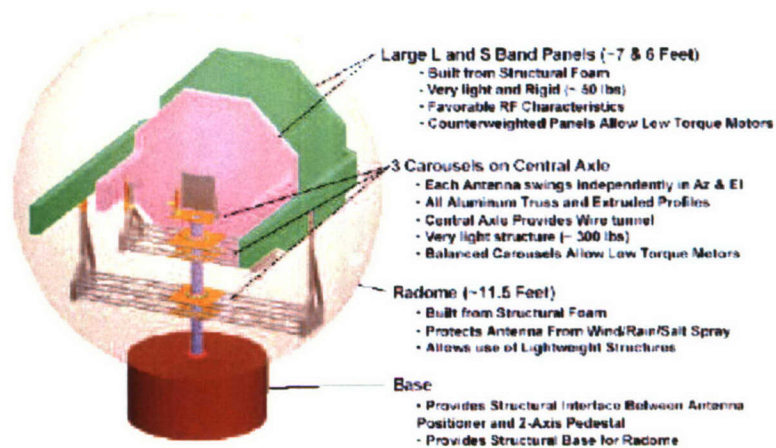


Figure 1.1 Geometry of the multi-band antennas system described in [2].

The S-band and L-band antennas are designed in printed technology and the ground plane is a frequency selective surface, transparent in the X-band (and in the S-band for the L-band antenna) and completely reflective in the operating frequency range of the antenna. Moreover, the radome covering this antenna system has also to be transparent in correspondence of those frequency bands. If the limitation of the antenna Radar Cross Section is an issue, the radome should be designed as a three-band FSS.

FSS-integrated feeding network can be used to design multi-band compact horn antennas.

Multi-band artificial magnetic conductors (AMC) can be obtained by placing a

multi-band FSS close to a ground plane. An AMC is designed for example to suppress surface waves, to act as thin absorbing screens or to enhance the performances of waveguide structures [3]. This type of AMC finds application in the sector of multi-band low-profile antennas for communication.

FSSs are also used as subreflectors for reflector antennas. In particular, for the Cassini project, a four-band FSS has been demonstrated in [4] which allows using the same reflector in Cassegrain configuration (for the X- and Ka-bands) and in prime focus configuration (for the S- and Ku-bands). For this type of applications a transmission and reflection band ratio $f_t/f_r < 1.7$ was required, together with angle and polarization independence.

The aim of the present project in the frame of the ITM program has been to develop the skills necessary for the design of multi-band FSSs associated to multi-band/wide band sensors. This required both studying the design solutions proposed so far in the open literature for achieving a multi-band behavior, and developing the capability to accurately characterise the performances of these designs. The first workpackage was devoted to the review of different multi-band FSSs configurations and to the comparison of their performances. The results of this study are outlined in Chap. 2.

Besides their strategic importance for military scenarios, multi-band FSSs are currently being considered also for civilian applications. For example, they are used to improve/limit wireless communication through building walls/windows. Such applications have been further investigated by an undergraduate student, in the frame of his Master final project, resulting on the design of a three-band FSS. The applied design procedure and the FSS performances are illustrated in Sec. 2.2. Although this work was performed outside the ITM program, a brief description is included in this report because it provides some guide lines for the design of multiband FSSs.

At TNO a software tool has been developed for the analysis of periodic passive arrays of metallic patches or apertures on a metallic plane, also when integrated with (active) waveguide arrays. This software has been successfully applied to the design of several FSSs. However, the tool can cope only with FSSs elements that can be discretised through a uniform rectangular mesh. As it will become clear from the literature review in Chap. 2, this represents a limitation in the design of multi-band FSSs for which complex non-rectangular element shapes are often needed. To overcome this limitation and enhance current design capabilities, the software tool has been equipped with a more general type of mesh and corresponding basis functions, suitable for any kind of element shape. A detailed description of their implementation in the adopted analysis technique is outlined in Chap. 3.2 together with some test cases considered for validation purposes.

Moreover, the tool was able to deal with arrays of elements located within the unit cell, but was not suitable for example for the analysis of generic grids (such as polarizers) or connected arrays. In the frame of this project, the continuity of the electric current at the edge of the unit cell has also been implemented. The applied methodology and the obtained results are described in Sec. 3.2.3.

Conclusions are drawn in Chap. 4 and recommendation for follow-up activities in the field of multi-band FSSs are provided.

2 Application of Multi-band FSSs

In Sec. 2 the most common applications for multi-band FSSs are reviewed. In Sec. 3 the design techniques proposed in literature for obtaining this type of FSS are briefly outlined.

2.1 Design Techniques for Multi-band FSSs

A multi-band FSS is characterised by multiple pass-bands and multiple stop-bands in the frequency range in which they are used. As mentioned in [5], two main approaches can be distinguished for the design of multi-band FSSs: multi-layer or stacked FSSs and single layer FSSs with multi-resonant elements. Furthermore, these two approaches can be implemented in different ways. A brief overview of the most common configurations is given in the following paragraphs.

2.1.1 Multi-layer or stacked FSSs

This configuration consists of the cascade of two or more FSSs, each one showing one of the required stop bands and being transparent at other frequencies. With respect to single-layer solutions, the stacked FSS is typically heavier and more complex to fabricate (requires bonding of the different layers). Since each layer can be designed with the periodicities that are most suited to achieve the desired frequency behaviour, the appearance of grating lobes can be avoided. A double-layer FSS designed for a reflector antenna is described in [4] and consists of a screen transparent in S- X- and Ku-bands and reflective in Ka-band, and another screen transparent in S- and Ku-bands and reflective in X-band, as shown in Fig. 2.1.

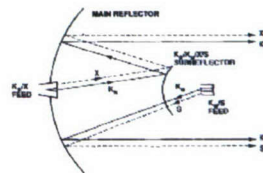


Figure 2.1 Four-bands FSS used as sub-reflector for the reflector antenna of the Cassini project [4].

2.1.2 Single-layer FSSs

The design of multi-band FSSs consisting of a single layer requires arranging on this layer either different elements with different resonance frequency or elements that show multiple resonance frequencies. The main advantages of this configuration with respect to the stacked FSS are low weight, limited volume occupation and limited dielectric losses (no need of separator between the different layers). However, the design requires in this case a more careful definition of the separation between the different elements: the spacing should be large enough to accommodate the different multi-resonant elements but still smaller than the value corresponding to the onset of grating lobes. These aspects will be discussed in more detail in the following paragraphs for the types of elements considered in this document.

2.1.2.1 Interlaced subarrays

The first approach results in interlaced subarrays and requires particular care in the choice of the elements and of the periodicities of each subarray.

As argued in [6], three aspects should be taken into account:

- higher order resonances of one type of element should not affect the stop-band produced by the other type of element and vice versa;
- the two subarrays should have regular periodicities;
- the periodicities should be such that no grating lobes occur in the operating frequency range of the entire FSS.

An example of interlaced subarrays, consisting of an array of conventional dipoles and an array of centrally loaded dipoles [6] is shown in Fig. 2.2.

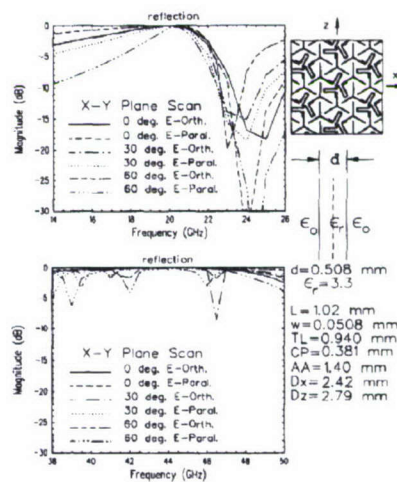


Figure 2.2 Single-layer dual band FSS, consisting of two subarrays of dipoles, as presented in [6].

2.1.2.2 Fractal FSSs

A fractal is obtained through a linear transformation of a simple geometry. The transformation consists of copying, scaling or translating the starting geometry and is applied iteratively to the entire resulting structure. If the iteration process is repeated a finite number of times, then the obtained structure is called prefractal, while the theoretical repetition for an infinite number of times leads to a fractal structure. A prefractal geometry consists then of elements showing an analogous frequency behaviour (since they have the same shape) but centred at different frequencies (because of the rescaling, the resonance frequency is also shifted), and it is therefore suitable for the design of multi-band arrays. The two types of fractals mainly investigated in literature as array elements are the Minkowski fractal, the Sierpinski carpet fractal and the Sierpinski dipole. Other types of fractal are often obtained as variations of these geometries.

The *Minkowski fractal element* is obtained by scaling the starting geometry and copying this scaled version on the corners of the element. Fig. 2.3 shows the Minkowski prefractal for the case of initial square element [8] and the corresponding transmission coefficient, both measured and simulated using two different simulation techniques: Method of Moments (MoM) and Finite-Difference-Time-Domain (FDTD). The structure shows two stop bands: the lowest corresponds to the resonance of the central square (primary patch), while the highest is due to the resonance of the squares at the corners (secondary

patches). However, these two resonances are not independent. As pointed out in [9], the secondary patches act as load for the primary patch and therefore they affect both the location of the first stop band and the ratio between stop bands.

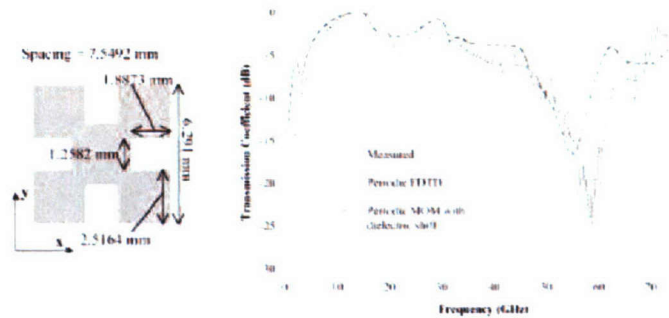


Figure 2.3 Minkowski prefractal element described in [8] for a dual-band FSS and corresponding transmission coefficient.

The *Sierpinski carpet fractal* consists of interlaced arrays whose elements are obtained by scaling the initial geometry. For example, the prefractal shown in Figure 3.5 was obtained by scaling a square patch of a quarter of its initial size and copying twelve of these scaled versions around the initial square. Also in this case, an array of these elements has two stop-bands: one corresponding to the resonance of the central square and the other to the resonance of the smaller copies as it appears from Fig. 2.4.

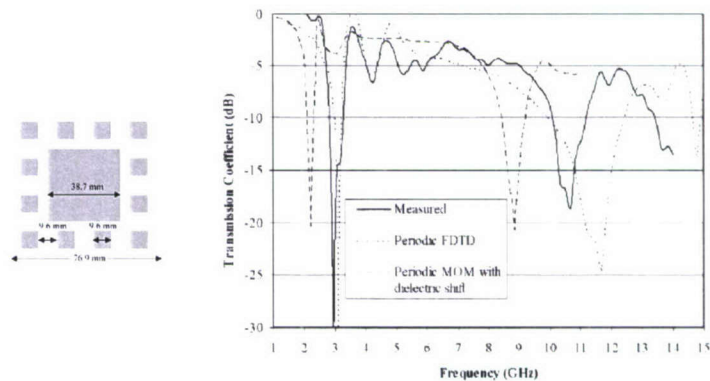


Figure 2.4 Sierpinski carpet prefractal element described in [8] and corresponding transmission coefficient.

Since the initial element and its copies are not touching, the two stop-bands can be designed more independently from each other than in the case of the Minkowski fractal element. The starting element of the *Sierpinski dipole* is a double triangle and looks similar to a bow-tie element. The pre fractal is obtained by rescaling the triangle and subtracting copies of the rescaled triangle from each of the two main triangles. For example, Figure 3.6 shows the transmission coefficient for a Sierpinski prefractal dipole resulting after five iterations with elements arranged in a triangular lattice. It has been shown in [5] that this configuration supports a maximum of two stop-bands. Just like for a general bow-tie element, the location of the two stop-bands (of the corresponding resonances) of the Sierpinski dipole can be tuned by acting on the flare angle, as shown in Fig. 2.5, while the ratio between the two bands remains the same. To apply this procedure to an FSS element, the spacing between adjacent elements should be sufficient to allow for a number of iterations. However, by enlarging this spacing (the array periodicities), the onset of grating lobes is anticipated and could affect the FSS

performances in the operating frequency range. Therefore, the derivation of a suitable prefractal element for the design of a multi-band FSS is the result of a trade-off between the avoiding the appearance of grating lobes and repeating the iteration process a sufficient number of times to obtain the desired multi-band behaviour.

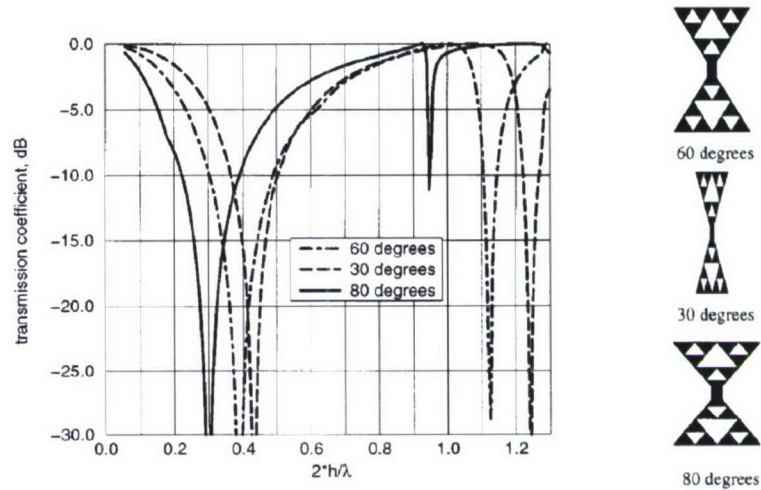


Figure 2.5 Transmission coefficient of the Sierpinski dipole for different values of the flare angle [5].

The *Inset Crossed dipole* proposed in [8] is a variation of the Sierpinski carpet with the initial element consisting of a crossed dipole instead of a square patch. This choice allows for arranging the element copies closer to each other, so that a third stop band can be obtained. However, the thickness of the dipole with respect to the periodicities of the initial array introduces a limitation on the maximum number of iterations of the fractal process (of nesting smaller crosses) and therefore to the maximum number of bands that can be obtained. Fig. 2.6 shows the fractal crossed dipole described in [8] and its reflection coefficient.

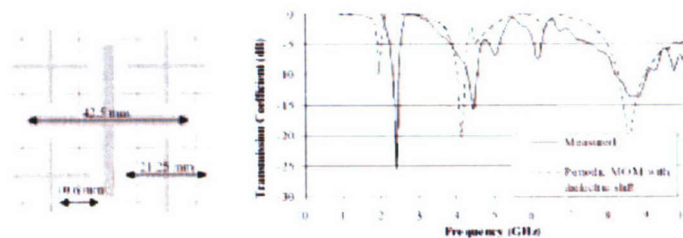


Figure 2.6 Inset Crossed dipole element proposed in [8] and corresponding transmission coefficient.

Summarizing, the main advantage of using fractal elements for multi-band FSSs is the possibility to obtain stop-bands that can be (almost) independently controlled. However, this type of elements has a fundamental design limitation: the maximum band separation depends on the size difference between primary and secondary elements, but the size of secondary elements is limited by the spacing between primary elements, which in turn determines the onset of grating lobes. In other words, an extra stop-band can be obtained by performing a new iteration only if the periodicity of the initial array is large enough to accommodate a new set of smaller secondary elements, but the onset of grating lobes sets an upper limit to these periodicities. Moreover, manufacturing constraints define the minimum element size that can be printed on the array substrate and therefore the

maximum number of iterations of the fractal process.

2.1.2.3 Bitmap FSSs

The limitations previously listed for interlaced subarrays and fractal FSSs can be overcome by considering unconventional element shapes, as those synthesized by applying a genetic algorithm (GA) [9, 10]. The first step consists in meshing a completely metallised array unit cell. Each mesh element, or pixel, can assume a value of 1 or 0 corresponding to the condition of completely metallised / not metallised pixel respectively (bitmapping [11]). A certain combination of values of the pixels of the entire cell constitutes a binary chromosome for the GA. A first set of chromosomes (population) is randomly generated and the fitness of each chromosome is evaluated against the desired array response. This evaluation requires calculating a cost function, which sets the desired filtering behaviour of the array in terms of reflection and transmission coefficient. The chromosomes are ranked on the basis of their fitness and the parents of the new generation are chosen by applying a tournament selection. The child chromosomes are then obtained by applying crossover and mutation. Elitism can also be introduced [12]. Just as the derivation of prefractal elements, also the application of a binary optimization algorithm, as for example GA, implies an iterative process. However, the GA might require a long computation time without reaching convergence, depending on the definition of the fitness function. Fig. 2.7 shows the element shape of an infra-red FSS designed to have two stop bands.

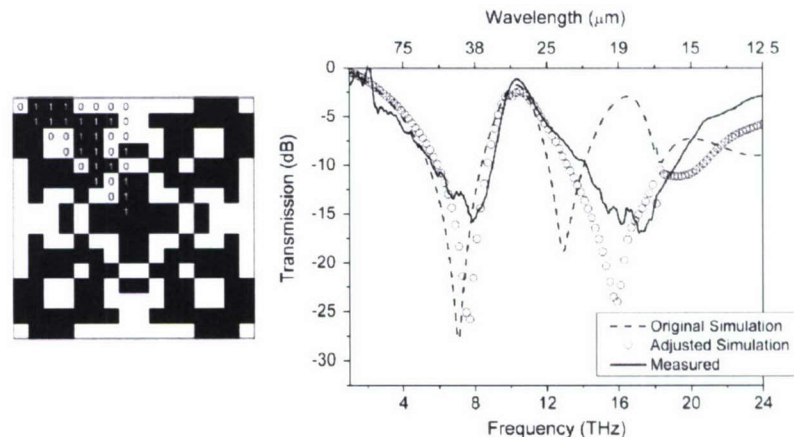


Figure 2.7 GA designed dual-band FSS described in [9].

Two main constraints limit the definition of new element shapes through the combined process of bitmapping and binary optimization. The manufacture accuracy defines the minimum size of the pixel that can be printed on the array substrate and therefore introduces an upper limit in the maximum mesh density. Moreover, the GA could arrive to configurations consisting of separate metallised areas connected only through a corner (diagonally connected pixels). This is the case for example of the geometry shown in Figure 3.11. These areas could not be manufactured as in the figure, and they would not be electrically connected. To overcome this problem the cell has to be trimmed, that is, simulated with higher pixel resolution (denser mesh) as shown in Fig. 2.8. In this case the manufacturing introduces a lower limit in the mesh definition.

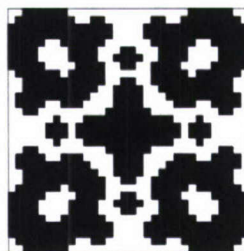


Figure 2.8 Trimmed version of the FSS unit cell shown in Fig. 2.8, [9].

2.2 A simple design case: an FSS window

The use of a very thin metallic coating in modern window design is an extremely effective way to save energy. Acting as a filter, the shielding blocks the electromagnetic radiation in the infrared region and is completely transparent to the visible part of the spectrum, thus rejecting the heat outside of a building during summer and keeping the heat inside during winter. These special windows are called low-emissivity (or energy saving) windows since the metallic oxide layer utilized reflects a significant portion of long and short infrared wave energy [16]– [18]. They are commercially available at large scale and used in many new buildings and vehicles. From a communication point of view, there is a subsequent problem with the use of such technology: the electromagnetic radiation in the microwave region is blocked and the blocking gets more intense as frequency increases. This means that wireless communication is severely restricted into and out from buildings. Hence, for GSM and Wireless Local Area Networks (LANs) use inside buildings, transparency is needed.

A solution to this problem is to create an FSS in the metallic coating of the low-emissivity glass, (Fig. 2.9). Such an FSS would consist of a periodic array of apertures obtained by removing the metallization from the window coating. It should be completely transparent at frequencies of GSM (900 MHz and 1800 MHz) and WiFi LAN (2400 MHz), without degrading the thermal response of the window. Therefore, the FSS should be designed to have three pass-bands in correspondence of these frequencies. Moreover, it should work for both polarizations and for all angles of incidence; the bandwidth required for these type of applications is rather narrow.

The planar two-dimensional periodic structure investigated in the frame of the final Master project of the student N. Fiscante is depicted in Fig. 2.10. It consists of two square loops and a crossed dipole centered in the elementary cell. Several simulations have been carried out to investigate how the transmission curves depend on the parameters of the elements, for different angles and different polarizations.

2.2.1 Low-emittance windows

As standard type of window pane, we have considered one described in [17]. It is made of non-magnetic glass with a typical conductivity of $\sigma = 10^{-12} \text{ S/m}$, a relative permittivity $\epsilon_r \approx 4$, and a thickness of $l \sim 4 \text{ mm}$. The pane presents no major obstacles to microwave radio propagation, since it is thin compared to the wavelength, and its conductivity is extremely small. The panes are transparent for more or less all radiation with frequencies below UV light. Thus, a window pane is transparent for visible light (390 – 770 nm), infrared (IR) light (770 – 2100 nm) as well as electromagnetic waves within the microwave region. The transparency of IR light is unfavourable during summer and winter. By using energy saving windows, one can improve thermal response

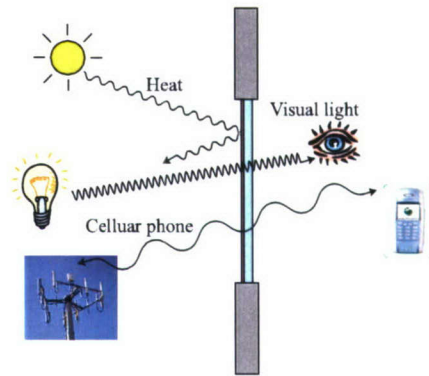


Figure 2.9 Illustration of how a frequency selective window works. The infrared radiation (heat) is blocked by the window, but the indoor outdoor communication is possible. The visible part of the spectrum remains unchanged [17].

leading to an economically viable solution. Low-emittance (low-e) windows consist of a microscopically thin, practically invisible coating deposited on the surface of the window pane. The coating is made of metal or metallic oxide and improves the thermal performance by reducing the solar heating, i.e., it reflects a significant portion of the infrared radiation. One drawback with these energy saving windows is the degrading of the radio channel properties.

There are two types of low-e windows: hard coat low-e and soft coat low-e. Hard coat low-e, or pyrolytic coating, is a coating applied at high temperatures and is sprayed onto the glass surface during the float glass process. The coating is relatively durable, which allows for ease of handling and tempering. Soft coat low-e, or sputter coating, is applied in multiple layers of optically transparent silver sandwiched between layers of metal oxide in a vacuum chamber. This process provides the highest level of performance and a nearly invisible coating, but is a more expensive alternative than the hard coat low-e glass.

2.2.2 Parametric studies

The parameters that can be optimized to shape the transmission response of the multi-band FSS in the microwave region are directly related to the FSS element itself. These include the elements length, width and periodicity. For the typical soft coat window, a relative permittivity of $\epsilon_r = 4$ and a glass thickness of 4 mm were assumed.

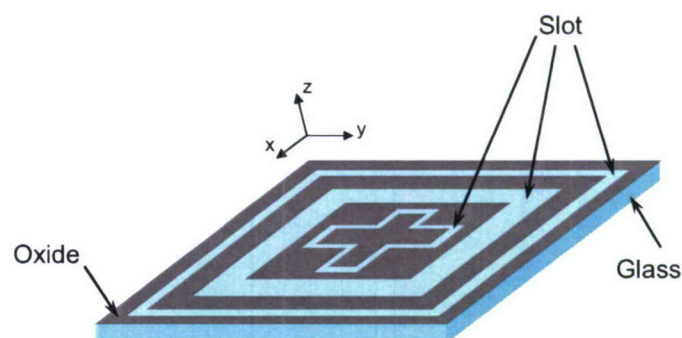


Figure 2.10 Unit cell of the frequency selective window.

The starting point in the design of a multi-element FSS is to calculate the approximate

wavelength at which the elements resonate. The square loop resonates approximately when its average circumference is equal to a multiple of the vacuum wavelength, $\lambda_0 = 2\pi r$ or $\lambda_0 = 2\pi(r + w)$ [7], where r is the average radius and w is the width of the loop. By adding a dielectric layer on one side of the FSS, the resonance f_0 is shifted downwards to approximately $f_0/\sqrt{(\epsilon_r + 1)/2}$ [4]. Hence, using the equality $\lambda_r = 2\pi r$, where λ_r is the wavelength in the medium with effective permittivity $\epsilon_{eff} = \sqrt{(\epsilon_r + 1)/2}$, a resonant frequency centered at 900 MHz yields a radius $r = 33.54 \text{ mm}$. The inner height of the first square loop is given by $2r = h\sqrt{2}$, hence $h = 47.44 \text{ mm}$. In the same way, considering a resonant frequency centered at 1800 MHz we obtain $h = 23.72 \text{ mm}$ for the second square loop. Finally, the FSS is made by a crossed loop element and has to resonate at 2400 MHz. The crossed element is particularly convenient because it allows achieving a certain resonance frequency with a total length which is less than half a wavelength as required for a resonating dipole. The development of this element is described in detail in [7] for the patch case, and illustrated in Fig. 2.11.

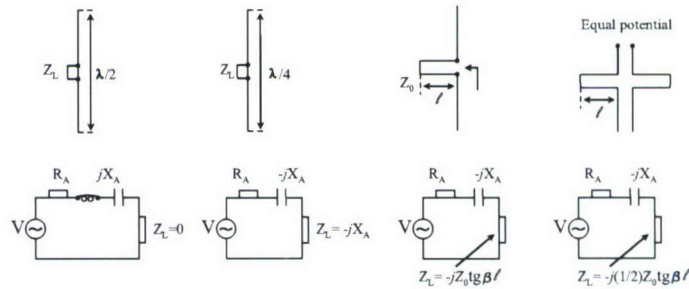


Figure 2.11 Development of the symmetric four-legged loop element starting from a $\lambda/2$ dipole.

At the frequency where the dipole length is $\lambda/2$, the dipole resonates and its radiation impedance is purely real. If the dipole is shorter, for example $\lambda/4$ long, then the radiation impedance is strongly capacitive and, to obtain resonance conditions (maximum current flow), the conductive part has to be matched with an inductive load. The load is obtained by using a two wire transmission line of length $\lambda/8$, terminated by a short circuit (the load impedance is then $Z_L = -jZ_0 \tan \beta\ell$). If two dipoles with this load are placed next to each other, the effective load impedance becomes half (parallel of the two load impedances). Moreover, since the tips of the two dipoles have the same potential, a short can be added without disturbing the field. By virtue of symmetry, this element resonates at almost the same frequency for both horizontal and vertical polarization, although it has a different 3 dB bandwidth for the reflection curves (narrower for the parallel than for the orthogonal polarization). The bandwidth of a periodic array of dipoles or slots can be adjusted by changing the array periods. However, this affects the frequency at which grating lobes occur. When using an array of four-legged loop elements, the bandwidth can be changed without affecting the resonance frequency of the structure and the occurrence of grating lobes. This is done by changing the distance between two dipoles: the larger the distance, the wider the bandwidth.

According to [7], this element will basically resonate when the largest tip-to-tip length is approximately equal to $\lambda_r/2$. Thus, for this case, we obtain $h = 19.77 \text{ mm}$. A width of the square loops and the cross element of $w = 1 \text{ mm}$ has been initially considered. The unit cell dimension is $51.45 \times 51.45 \text{ mm}^2$ to avoid the presence of grating lobes.

Fig. 2.12 plots the transmission response for TE and TM polarization varying the incidence angle: $\vartheta \in [0^\circ - 60^\circ]$, obtained using Ansoft Designer, a Method of Moment commercial code. As expected, the entire structure shows the multi-band behavior, so

that it is transparent at the desired frequencies. It is important to note that once the three elements are put together, in the configuration shown in Fig. 2.10, the mutual coupling introduces a shift in the resonant frequency of each element. As a consequence, the parameters of the elements, i.e., the length and the width, had to be properly tuned. Tab. 2.1 shows the new parameter values.

2.2.3 The effect of varying the angle of incidence

It is shown in Fig. 2.12, that as the incidence angle increases, an unexpected peak of the transmission coefficient appears around 2.1 GHz. Moreover, this peak is more evident for TE than TM polarization.

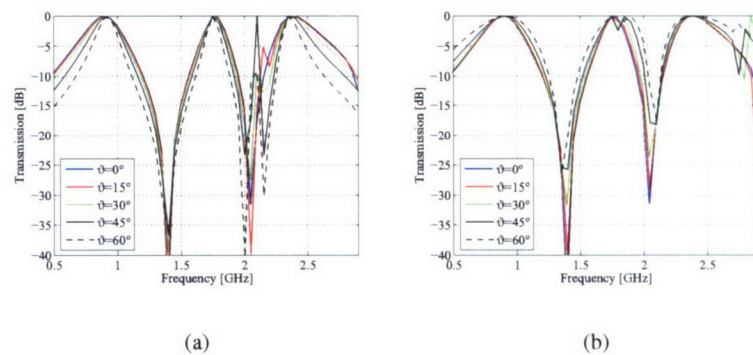


Figure 2.12 Transmission response of the frequency selective window for different incidence angles and polarizations. TE-polarized wave (left). TM-polarized wave (right).

To understand the origin of this peak, the three FSS elements in the unit cell shown in Fig. 2.10, have been separately simulated for TE and TM polarization. The results are shown in Fig. 2.13. For the external loop (square loop₁), we can observe a peak of the transmission coefficient for all angles of incidence but not for normal incidence at about 1.8 GHz for TM polarization and 2.1 GHz for TE polarization. A second unexpected peak appears at about 3 GHz for both polarizations and for all angle of incidence, here including also perpendicular incidence. From Fig. 2.13 we can see that the internal loop (square loop₂) presents only one peak of the transmission coefficient in the considered frequency range, at about 3.2 GHz this peak has the same characteristics as the first peak observed for the external loop. Finally, the transmission coefficient of the crossed loop does not show any anomalous peak. This allow us to exclude that the peaks observed for the two square loops are due to grating lobes, which only depend on incidence direction, frequency and unit cell geometry, and should therefore appear for any element shape and any polarization. Moreover, it can be easily verified that for the considered frequency range the structure does not support surfaces wave modes.

To explain the nature of this peak, in [19] an expansion of the currents induced on the square loop in terms of sinusoidal functions has been proposed. According to this

| | h_i [mm] | w_i [mm] |
|--------------------------|------------|------------|
| Square loop ₁ | 45.75 | 1.25 |
| Square loop ₂ | 27.00 | 3.00 |
| Cross element | 22.00 | 1.00 |

Table 2.1 Parameters values for the three elements of the multi-band FSS.

expansion the resultant current distribution on the loop is plotted in Fig. 2.14a and Fig. 2.15a for $\vartheta = 0^\circ$, $f = 0.9$ GHz and $\vartheta = 60^\circ$, $f = 2.1$ GHz, respectively. Fig. 2.14b and 2.15b show the current distribution as obtained as Ansoft Designer. The main resonance at 0.9 GHz can therefore be interpreted as the resonance of the structure formed by the symmetrical halves around the vertical axis of symmetry of the square loop. A resonance of the four corners occurs at about double frequency, due to the excitation of the first odd modes. Odd modes can be excited only for oblique angles of incidence. The second anomalous peak in Fig. 2.13 for the square loop corresponds to the resonance of the first even higher order mode.

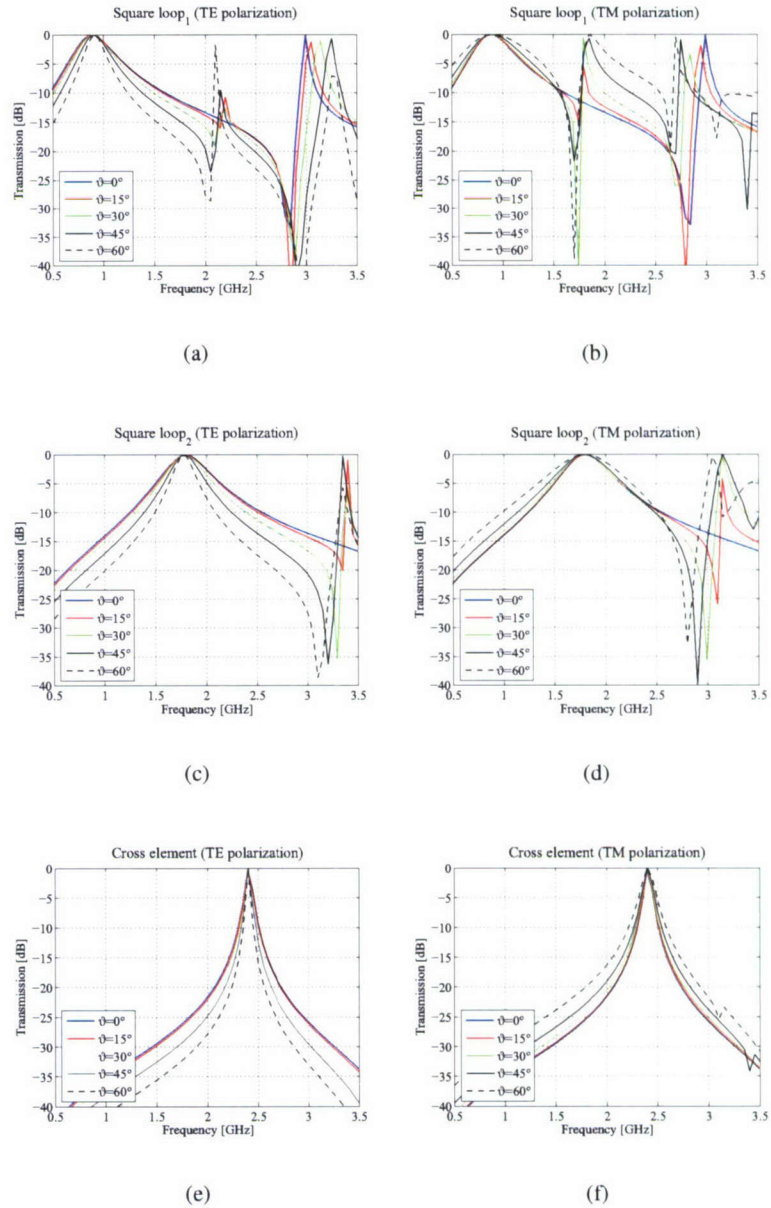


Figure 2.13 The effect of variations in the incidence on shielding effectiveness of the square loops and the cross element.

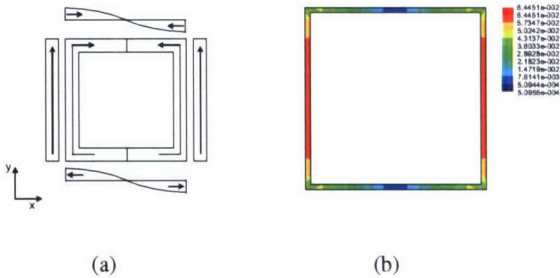


Figure 2.14 Current distribution for $f = 900 \text{ MHz}$ and $\vartheta = 0^\circ$ for TE-polarized wave according to [19] (a) and Ansoft Designer (b). Arrows shows directions of current flow.

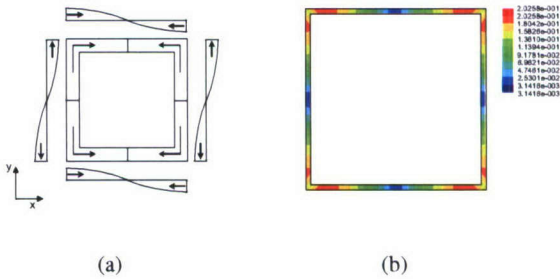


Figure 2.15 Current distribution for $f = 2.1 \text{ GHz}$ and $\vartheta = 60^\circ$ for TE-polarized wave according to [19] (a) and Ansoft Designer (b). Arrows shows directions of current flow.

3 Upgrades to the IEMEN analysis technique

3.1 Introduction

In general the design of an FSS is performed in two phases. During the first phase, starting from the analysis of the requirements, a preliminary design is obtained by acting on the physical parameters that determine the behaviour of multi-layer periodic arrays (number of layers, thickness and permittivity of dielectric substrates and separators, array periodicity, arrays element shape and size) [13]. The obtained configuration usually represents a suboptimal solution of the design problem. In a second phase, this solution is optimised by fine tuning those same parameter values. Optimisation algorithms offer a structured and controlled way to perform this tuning and have become an essential instrument in electromagnetic design. This is particularly important for the design of complex elements, such as those required for multi-band FSSs, since they involve the variation of a relatively large number of parameters. All the configurations described in Section 2, both for the case of multi-layer FSS and single-layer FSS, offer several advantages and suffer from some problems. The choice of the particular configuration is strictly related to the particular application to be considered and on the specific requirements set on the FSS, as already observed in a similar study performed on multi-function arrays [14]. Therefore, it is important to be able to design and optimise each of these configurations.

The software tool TwoDim, developed at TNO for the analysis of multi-layer periodic structures, has already been successfully applied to the design of several multi-layer FSSs. The software is the result of the implementation of the Multimode Equivalent Network approach based on the Integral Equation formulation (IEMEN), a method initially proposed for waveguide arrays and subsequently extended to the analysis of patch- and slot-based FSSs [13]. The formulation is centred on a single integral equation with a fixed kernel, containing only localised modes (reduced kernel), and with multiple forcing terms, one for each accessible mode. The integral equation is solved by applying the Method of Moments with a Galerkin formulation. The basis and test functions currently implemented are sub-domain piece-wise linear and piece-wise sinusoidal based on a uniform rectangular mesh. Consequently, only shapes obtained as combination of rectangular elements can be simulated, with the length and width of these elements being discretised in terms of the length and width of the functions:

$$l_{tot} = l_{fun}(n + 1)$$

where l_{tot} is the element length and l_{fun} is the function length. Moreover, in order to correctly represent the induced electric or magnetic current at the cross points between these elements, the basis functions on the crossing elements should be arranged to have their maximum in correspondence of these cross points. Therefore, the lengths of crossing elements cannot be independently varied. These geometrical constraints limit the shapes and dimension of elements that can be simulated and do not allow us to explore all the possible solutions for a certain design problem. Furthermore, because of the dependence of shape parameters in the geometry definition implemented in TwoDim (length and width of rectangular elements), we cannot fully benefit from the application of an optimization algorithm. To tackle this problem, a non-uniform mesh should be considered and more general basis functions should be implemented, such as for example the Rao Wilton Glisson functions (RWG) introduced in [21].

The bitmapping procedure mentioned in Chap. 2 has partially been implemented in the

software in the frame of another project, but to be efficiently used for the synthesis of an FSS element it still needs to be connected to the optimization loop. Moreover, to have maximum freedom in the design, the optimization should start from a completely metallized unit cell. For this purpose, a method should be identified such that the software tool ensures the continuity of the equivalent electric currents at the border between two cells.

The two mentioned issues entail two major upgrades in the software. The study and implementation of RWG functions has been given the priority since it provides TNO software tool with the flexibility needed for the synthesis of multi-band FSSs. The corresponding activities have been performed by a graduate student from the University of Turin (Italy) in the frame of a six-month internship at TNO, following these steps:

- 1a Study the IEMEN formulation and get acquainted with the TwoDim software tool;
- 1b Identify a general non-uniform mesh and establish an architecture for the mesh description;
- 1c Study the RWG functions and implement them as basis and test functions using the chosen mesh;
- 1d Test the software with the new implementation.

The implementation of the continuity of the currents at the border of the unit cell required:

- 2a Identify a suitable methodology to ensure that electric currents on elements placed between two unit cells are continuous;
- 2b Implement the methodology in the software tool;
- 2c Test the software with the new implementation.

3.2 Rao Wilton Glisson functions

3.2.1 Formulation of the problem

The Twodim code for the FSS analysis is based on the IEMEN formulation described in [13]. This technique, starting from a modal expansion of the fields in each layer, provides equivalent microwave networks, that are cascaded to represent the entire structure. These equivalent networks are obtained by solving an electric field integral equation for patch-based FSSs, or a magnetic field integral equation for aperture-based FSSs. The integral kernel of this equation is written in terms of modes, that are separated in accessible and non accessible modes. Accessible are the modes that contribute to the interaction between adjacent discontinuities, i.e. the propagating modes and the evanescent modes that are not attenuated above a chosen threshold. As a result of the separation, we obtain a single integral equation, with fixed kernel and multiple forcing terms (the extracted Floquet modes). For instance for a patch-based FSS the IE (Integral Equation) is in the following form:

$$\mathbf{e}_i(\mathbf{r}_t) = - \int_{cell} \mathbf{G}_{na}^e(\mathbf{r}_t; \mathbf{r}'_t) \cdot \mathbf{J}_i(\mathbf{r}'_t) d\mathbf{r}'_t \quad (3.1)$$

where \mathbf{e}_i is the extracted Floquet mode ($i = 1 \dots N_a$, N_a being the number of accessible modes), \mathbf{G}_{na}^e is the non-accessible Green's function, and \mathbf{J}_i is the equivalent superficial current density.

To solve the obtained IE the Method of Moments is used. Firstly the unknown current densities are discretised as a linear combination of a set of chosen basis functions:

$$\mathbf{J}_i(\mathbf{r}_t) = \sum_{m=1}^N I_m^{(i)} \mathbf{f}_m(\mathbf{r}_t) \quad (3.2)$$

Then the testing procedure is applied: the discretised IE is tested on a chosen set of test functions, which corresponds to the minimization of the projection of the residual over each test function. With Galerkin's choice the set of test functions is the same set of the basis functions.

$$\int_{cell} \mathbf{e}_i(\mathbf{r}_t) \cdot \mathbf{f}_n(\mathbf{r}_t) = - \sum_{m=1}^N I_m^{(i)} \int_{cell} d\mathbf{r}_t \mathbf{f}_n(\mathbf{r}_t) \cdot \int_{cell} d\mathbf{r}'_t \mathbf{f}_m(\mathbf{r}'_t) \cdot \mathbf{G}_{na}^e(\mathbf{r}_t; \mathbf{r}'_t) \quad (3.3)$$

Thus we have reduced the integral equation into an algebraic linear system (with one different forcing term for each accessible mode), that can be expressed in a more compact form:

$$\begin{aligned} \mathbf{Z} \mathbf{I}^{(i)} &= \mathbf{V}^{(i)} \\ Z_{mn} &= - \int_{cell} d\mathbf{r}_t \mathbf{f}_n(\mathbf{r}_t) \cdot \int_{cell} d\mathbf{r}'_t \mathbf{f}_m(\mathbf{r}'_t) \cdot \mathbf{G}_{na}^e(\mathbf{r}_t; \mathbf{r}'_t) \\ V_n^{(i)} &= \int_{cell} \mathbf{e}_i(\mathbf{r}_t) \cdot \mathbf{f}_n(\mathbf{r}_t) \end{aligned}$$

Then the Green's function is expressed in terms of Floquet modes, and the reaction integrals Z_{mn} can be rewritten in the following form:

$$Z_{mn} = - \frac{1}{d_x d_y} \sum_{p=N_a+1}^{\infty} \mathbf{G}_{na}(\mathbf{k}_p) \cdot \int_{cell} d\mathbf{r}_t \mathbf{f}_n(\mathbf{r}_t) \cdot \int_{cell} d\mathbf{r}'_t \mathbf{f}_m(\mathbf{r}'_t) e^{-j\mathbf{k}_p \cdot (\mathbf{r} - \mathbf{r}')}$$

The Fourier integrals in the expression above can be straightforwardly identified, which leads to the following expression:

$$Z_{mn} = - \frac{1}{d_x d_y} \sum_{p=N_a+1}^{\infty} \mathbf{F}_n(-\mathbf{k}_p) \cdot \mathbf{G}_{na}(\mathbf{k}_p) \cdot \mathbf{F}_m(\mathbf{k}_p) \quad (3.4)$$

Similarly if we make the Fourier exponential explicit in the forcing terms we may rewrite:

$$V_n^{(i)} = \mathbf{e}'_i \cdot \mathbf{F}_n(-\mathbf{k}_i) \quad (3.5)$$

Thus we need to evaluate an infinite series for each entry of the MoM matrix. The problem is of course the slow rate of convergence of this series, which determines the computational times of the IEMEN method. To increase the rate of convergence the Kummer transformation is applied: the asymptotic term (i.e. for large values of k_x and k_y) of the series is added and subtracted:

$$\begin{aligned}
Z_{mn} = & - \frac{1}{d_x d_y} \sum_{p=N_a+1}^{\infty} \mathbf{F}_n(-\mathbf{k}_p) \cdot [\mathbf{G}_{na}(\mathbf{k}_p) - \mathbf{G}_{na}^a(\mathbf{k}_p)] \cdot \mathbf{F}_m(\mathbf{k}_p) + \\
& - \frac{1}{d_x d_y} \sum_{p=N_a+1}^{\infty} \mathbf{F}_n(-\mathbf{k}_p) \cdot \mathbf{G}_{na}^a(\mathbf{k}_p) \cdot \mathbf{F}_m(\mathbf{k}_p)
\end{aligned} \tag{3.6}$$

where $\underline{\underline{G}}_{na}^a$ is the asymptotic Green's function, and it is shown in [20] that the Green's function of stratified media tends to the homogenous media Green's function with dielectric constant equal to the average of the closest media dielectric constants. Thus we have two terms in the MoM matrix: the former term is a series with faster rate of convergence than the original series, the latter is a reaction integral which can be efficiently evaluated in the spatial domain, after applying inverse Poisson transformation.

3.2.1.1 Basis functions

Twodim has been originally implemented with support for piece-wise linear functions (also known as rooftop functions), which are well-suited for the modeling of geometries that conform to Cartesian coordinates. Rooftop functions however impose some limitations on the kind of structures that can be analyzed. In fact they can discretize only rectangular-shaped structures. Moreover in the Twodim implementation the mesh must be uniform, which means that if we want to refine the mesh in certain areas (typically in proximity of corners) we have to refine the entire mesh. Furthermore a rooftop function has the same vectorial direction in every point, which means that the current will assume that same direction. Therefore for generic problems we need to overlap two orthogonal rooftop functions, so we need to double the number of unknowns.

To go beyond these limitations we have introduced in Twodim the support for more flexible basis functions, which are the functions from the set introduced in 1982 by Rao, Wilton and Glisson (see [21]). Each one of these functions (which we will refer to as RWG functions) is defined on a pair of adjacent triangles, which have a common edge, and do not need to be coplanar. Referring to the quantities defined in Fig. 3.1 we define the RWG function as follows:

$$\underline{f}_n(\underline{r}) = \begin{cases} \frac{l_n}{A_n^+} \rho_n^+ & \text{when } \mathbf{r} \in T_n^+ \\ \frac{l_n}{A_n^-} \rho_n^- & \text{when } \mathbf{r} \in T_n^- \\ 0 & \text{otherwise} \end{cases} \tag{3.7}$$

with A_n^\pm the area of the triangle T_n^+ or T_n^- . These functions do not present the disadvantages of rooftop functions: they are suited to model arbitrary shaped geometries, even non planar structures (this is not the case of FSSs of course). Furthermore they allow to represent arbitrary currents. Since the mesh is not uniform we can mesh the structure with better detail in proximity of critical points, like corners.

Then, the necessary steps in order to make Twodim compatible with a triangular mesh are the following:

- generating a suitable description of the RWG functions from the output of the mesher;
- efficiently evaluating spatial Fourier transforms of RWG functions;
- evaluating spatial couplings.

At present the code supports the output files from GiD and Ansys Workbench, but it can be easily upgraded to different file formats. Fig. 3.2 illustrates the mesh obtained with

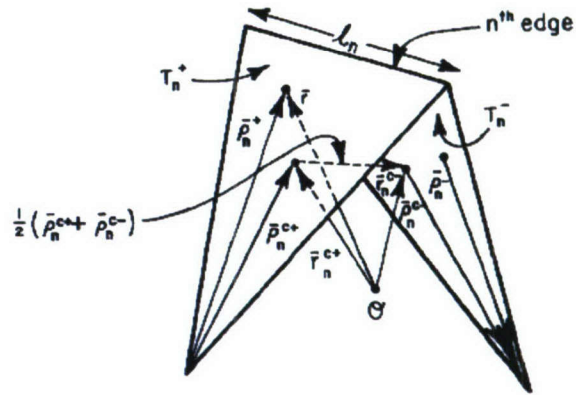


Figure 3.1 Triangle pair and geometrical parameters associated with interior edge.

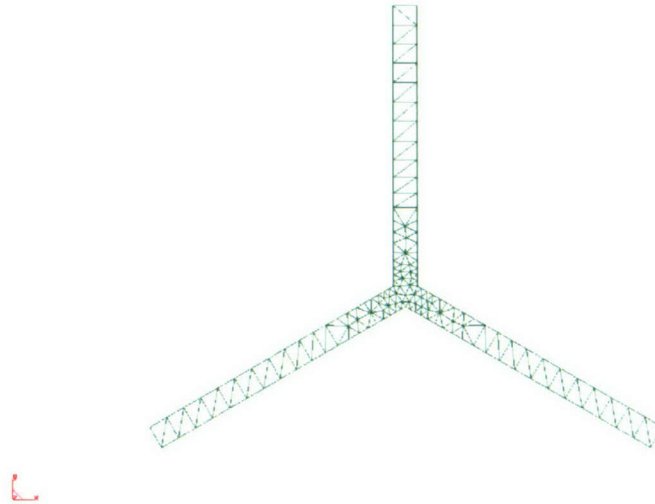


Figure 3.2 Unloaded tripole.

GiD software for a simple tripole. This tripole could not be meshed with rooftop functions because of the non-right angles. Furthermore it is possible to notice that the mesh is thinner near the junction of the three dipoles than in the middle of the arms, which would not have been possible using a rectangular mesh.

3.2.1.2 Fourier transforms of RWG functions

The algorithm implemented in the code is the algorithm described in [22]. After splitting the integration over the two triangles T^\pm , each integration domain is mapped onto a reference right triangle with unitary catheti lying on the coordinate axes, as graphically illustrated in Fig. 3.3.

To accomplish the mapping (for instance for the triangle T^+) a change of variables is performed:

$$\mathbf{r} = \mathbf{r}_{3+} + \mathbf{J}_+ \cdot \tilde{\mathbf{r}} \quad (3.8)$$

with

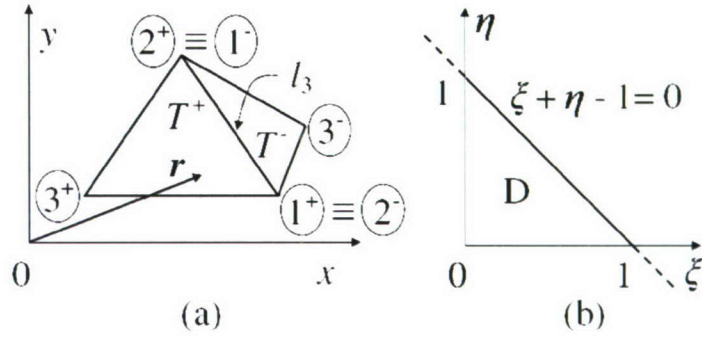


Figure 3.3 Computation of the Fourier transform of a RWG function defined over a generic triangle pair (a) is reduced to an integral over a standard right triangle (b).

$$\tilde{\mathbf{r}} = \begin{bmatrix} \xi \\ \eta \end{bmatrix}, \quad \mathbf{J}_+ = \begin{bmatrix} x_{1+} - x_{3+} & x_{2+} - x_{3+} \\ y_{1+} - y_{3+} & y_{2+} - y_{3+} \end{bmatrix}$$

The new variables ξ and η are commonly known in literature as *area coordinates*. Applying this change of variables to the integral which defines the Fourier transform one obtains:

$$\begin{aligned} \iint_{T^+} \mathbf{f}^+(\mathbf{r}) e^{j\mathbf{k}_t \cdot \mathbf{r}} d\mathbf{r} &= \iint_D \mathbf{f}^+(\tilde{\mathbf{r}}) e^{j\mathbf{k}_t \cdot \mathbf{J}_+ \cdot \tilde{\mathbf{r}}} |\mathbf{J}_+| e^{j\mathbf{k}_t \cdot \mathbf{r}_{3+}} d\tilde{\mathbf{r}} = \\ &= l_3 e^{j\mathbf{k}_t \cdot \mathbf{r}_{3+}} \mathbf{J}_+ \cdot \iint_D \begin{bmatrix} \xi \\ \eta \end{bmatrix} e^{j\tilde{\mathbf{k}}_t \cdot \tilde{\mathbf{r}}} d\tilde{\mathbf{r}} \end{aligned} \quad (3.9)$$

where

$$\tilde{\mathbf{k}}_t = \begin{bmatrix} \tilde{k}_x & \tilde{k}_y \end{bmatrix} = \mathbf{k}_t \cdot \mathbf{J}_+, \quad |\mathbf{J}_+| = 2A^+$$

with $|\bullet|$ being the determinant. The two integrals appearing in eq. 3.9 can be analytically evaluated by introducing an auxiliary function Ψ :

$$\Psi(x) = \frac{e^{jx} - 1}{jx} \quad (3.10)$$

With the aid of this function we can express the integrals appearing in eq. 3.9 as follows:

$$\iint_D \begin{bmatrix} \xi \\ \eta \end{bmatrix} e^{j\tilde{\mathbf{k}}_t \cdot \tilde{\mathbf{r}}} d\tilde{\mathbf{r}} = - \begin{bmatrix} \frac{\partial}{\partial \tilde{k}_x} \\ \frac{\partial}{\partial \tilde{k}_y} \end{bmatrix} \frac{\Psi(\tilde{k}_x) - \Psi(\tilde{k}_y)}{\tilde{k}_x - \tilde{k}_y} \quad (3.11)$$

The derivative with respect to \tilde{k}_x is given by:

$$-\frac{\partial}{\partial \tilde{k}_x} \frac{\Psi(\tilde{k}_x) - \Psi(\tilde{k}_y)}{\tilde{k}_x - \tilde{k}_y} = \frac{\Psi(\tilde{k}_x) + (\tilde{k}_y - \tilde{k}_x) \frac{d\Psi(\tilde{k}_x)}{d\tilde{k}_x} - \Psi(\tilde{k}_y)}{(\tilde{k}_y - \tilde{k}_x)^2} \quad (3.12)$$

The derivative with respect to \tilde{k}_y follows by interchanging \tilde{k}_x and \tilde{k}_y . The derivative appearing in 3.12 seems singular when $\tilde{k}_x \rightarrow \tilde{k}_y$. However the singularity is only

apparent (i.e. removable), which can be proven by expanding eq. 3.12 with its Taylor series. Although the singularity is only apparent, a direct implementation of the formula would be numerically unstable, and the results would not be accurate. Thus we expanded the formulas involving the function Ψ and its derivatives with appropriate Taylor series. We have to distinguish the cases when both \tilde{k}_x and \tilde{k}_y tend to zero, and when $\tilde{k}_x \rightarrow \tilde{k}_y$ but they are not close to zero:

$$\frac{\Psi(\tilde{k}_x) + (\tilde{k}_y - \tilde{k}_x) \frac{d\Psi(\tilde{k}_x)}{d\tilde{k}_x} - \Psi(\tilde{k}_y)}{(\tilde{k}_y - \tilde{k}_x)^2} = \begin{cases} \frac{1}{6} + \sum_{n=1}^{\infty} \frac{j^n}{(n+3)!} \left[(n+1)\tilde{k}_x^n + \sum_{p=1}^{n-1} (n-p+1)\tilde{k}_x^{n-p}\tilde{k}_y^p + \tilde{k}_y^n \right] & \text{when } \tilde{k}_x, \tilde{k}_y \rightarrow 0 \\ - \sum_{n=0}^{\infty} \frac{1}{(n+2)!} \Psi^{(n+3)}(\tilde{k}_x) (\tilde{k}_y - \tilde{k}_x)^n & \text{when } \tilde{k}_x \rightarrow \tilde{k}_y \neq 0 \end{cases} \quad (3.13)$$

with the n-th derivative of the function Ψ known in a closed form:

$$\Psi^{(n)}(x) = \frac{d^n \Psi(x)}{dx^n} = j(-1)^{n+1} n! \frac{e^{jx-1}}{x^{n+1}} + j(-1)^{n+1} e^{jx} \sum_{k=1}^n (-j)^k \frac{n!}{k!} \frac{1}{x^{n-k+1}} \quad (3.14)$$

In the present implementation 8 terms have been included in the series expansions, and a threshold equal to 10^{-2} has been used. With these preliminaries in hand, the Fourier transform of $\mathbf{f}^+(\mathbf{r})$ can be written as:

$$\iint_{T^+} \mathbf{f}^+(\mathbf{r}) e^{j\mathbf{k}_t \cdot \mathbf{r}} d\mathbf{r} = l_3 e^{j\mathbf{k}_t \cdot \mathbf{r}_{3+}} \mathbf{J}_+ \cdot \begin{bmatrix} \frac{\Psi(\tilde{k}_x) + (\tilde{k}_y - \tilde{k}_x) \frac{d\Psi(\tilde{k}_x)}{d\tilde{k}_x} - \Psi(\tilde{k}_y)}{(\tilde{k}_y - \tilde{k}_x)^2} \\ \frac{\Psi(\tilde{k}_y) + (\tilde{k}_x - \tilde{k}_y) \frac{d\Psi(\tilde{k}_y)}{d\tilde{k}_y} - \Psi(\tilde{k}_x)}{(\tilde{k}_x - \tilde{k}_y)^2} \end{bmatrix} \quad (3.15)$$

Finally the transform of $\mathbf{f}^-(\mathbf{r})$ can be analogously computed, after defining the variable change:

$$\mathbf{r} = \mathbf{r}_{3-} + \mathbf{J}_- \cdot \tilde{\mathbf{r}}, \quad \mathbf{J}_- = \begin{bmatrix} x_{1-} - x_{3-} & x_{2-} - x_{3-} \\ y_{1-} - y_{3-} & y_{2-} - y_{3-} \end{bmatrix}$$

The result will be formally the same, except for a change in sign. The complete Fourier transform is simply the sum of the contributes over the two triangles.

3.2.2 Spatial asymptotic term

Recalling eq. 3.6 and applying inverse Poisson transformation to the asymptotic term, we can express this term in the spatial domain as follows (see [20]):

$$Z_{mn}^a = e^{-jk_{x0}(x_m-x_n)} e^{-jk_{y0}(y_m-y_n)} \frac{1}{d_x d_y} \sum_{n_x=-\infty}^{\infty} \sum_{n_y=-\infty}^{\infty} r_a(n_x, n_y)$$

where

$$\begin{aligned} r_a(n_x, n_y) &= \left\langle \mathbf{f}_i, \underline{\mathbf{g}}_a * \mathbf{f}_j(n_x, n_y) \right\rangle = \\ &= \int_{\Sigma_i} \int_{\Sigma_j} \mathbf{f}_i(x, y) \underline{\mathbf{g}}_a(x, y; x', y') \mathbf{f}_j(x', y'; n_x, n_y) d\Sigma d\Sigma' \end{aligned} \quad (3.16)$$

$\mathbf{f}_j(x', y'; n_x, n_y)$ represents the j -esime RWG function defined in the base cell and translated in the cell with indices n_x and n_y . Therefore we have to deal with a series of double surface integrals over the domains of the basis functions (i.e. triangular domains).

Considering the case of a periodic source, it is shown in [20] that the extracted asymptotic term of the Green's function can be written in the following form:

$$\underline{\mathbf{g}}_a(x, y; x', y') = -j \frac{c}{2\pi} \begin{bmatrix} -\frac{\partial^2}{\partial x \partial x'} & -\frac{\partial^2}{\partial x \partial y'} \\ \frac{\partial^2}{\partial y' \partial x'} & -\frac{\partial^2}{\partial y \partial y'} \end{bmatrix} \frac{e^{-juR}}{R} = j \frac{c}{2\pi} \nabla \nabla' \frac{e^{-juR}}{R} \quad (3.17)$$

where u is the smoothing parameter, and R is the distance between source and observation points.

RWG functions have a property which can be exploited to simplify the above integrals. Since each function has no component normal to the boundary, making use of a surface vector calculus identity lets us transfer the divergence from the Green's function to the basis functions. Then eq. (3.16) becomes:

$$r_a(n_x, n_y) = j \frac{c}{2\pi} \int_{\Sigma_i} d\Sigma \nabla \cdot \mathbf{f}_i(x, y) \int_{\Sigma_j} d\Sigma' \frac{e^{-juR}}{R} \nabla \cdot \mathbf{f}_j(x', y'; n_x, n_y) \quad (3.18)$$

The divergence of RWG functions is constant over each triangle:

$$\nabla \cdot \mathbf{f} = \begin{cases} \frac{l}{A^+} & \mathbf{r} \text{ in } T_n^+ \\ -\frac{l}{A^-} & \mathbf{r} \text{ in } T_n^- \\ 0 & \text{otherwise} \end{cases} \quad (3.19)$$

Consequently, the integral of eq. (3.18) involves only the free space Green's kernel. Since each surface Σ_i consists of two triangles the integral can be decomposed as a sum of four integrals over four different pairs of triangles. Each of these integrals has the following form (neglecting the constant term $j \frac{c}{2\pi}$):

$$\frac{l_i l_j}{A_i^\pm A_j^\pm} \int_{\Sigma_i^\pm} d\Sigma \int_{\Sigma_j^\pm} d\Sigma' \frac{e^{-juR}}{R}$$

where the dependence on n_x and n_y is taken into account by translation of the domain of the internal integral, which of course reflects on R .

When evaluating this kind of integral we have to consider three different cases:

- 1 the two domains of integrations (i.e. the triangles) are *far enough* (usually $\lambda/4$);
- 2 the two domains are near, and we need to be careful because of the proximity of Green's function singularity;
- 3 the two domains actually are the same domain (i.e. coincident triangles).

3.2.2.1 Far triangles

The distance between the triangles is approximated by the distance between their baricenters (for a more accurate analysis we should take into account also the dimensions of the triangles). Then this distance is compared to a threshold, which is chosen equal to $\lambda/4$, where λ is not the actual wavelength, but it is an *equivalent* wavelength extracted from the smoothing parameter u . If the distance is greater than the threshold, then we are far enough from the Green's function singularity, and the integrand has a regular behavior. In view of this we can use Gaussian quadrature rules, which corresponds to a polynomial approximation of the Green's function. To be more specific, we use a rule of degree 1 with 1 point for the external integral, and a rule of degree 5 with 7 points for the internal integral. These rules, as well as the following ones, can be found in [23].

3.2.2.2 Near triangles

When the distance between the two domains of integration is less than the threshold, we have to be careful using quadrature rules because of the $\frac{1}{R}$ singularity. The most common approach consists in splitting the integrand in a regular part and a singular part. The regular part does not present a singularity and therefore can be integrated with standard Gaussian rules. The singular part can be handled analytically since closed forms for the integral exist.

$$g(R) = g_{sing}(R) + g_{reg}(R) = \frac{1}{R} + \frac{e^{-juR} - 1}{R} \quad (3.20)$$

The singularity of the second term is only apparent (i.e. removable), which can be proved by calculating the limit:

$$\lim_{R \rightarrow 0} g_{reg}(R) = \lim_{R \rightarrow 0} \frac{e^{-juR} - 1}{R} = -ju$$

For computing the integral we use a Gaussian rule of degree 7 with 16 points for the external integral, while the internal integral is evaluated with a degree 1 rule with 1 point for the regular term, while an analytical formulation exists for the singular term [25].

3.2.2.3 Coincident triangles

The case of coincident triangles is a particular case of the previous one, but requires a different handling. For the regular term we could use the same numerical rule on the external and internal integrals, since no singularity exists (which means that we could even use a rule that samples the integrand in $R = 0$, as happens if the rule for the two integrals is the same). Though it is demonstrated (see [24]) that a more accurate result is achieved by a seven point formula of fifth degree (Stroud) and a nine points formula of degree three (Stroud's 3 points formula modified by Graglia). We have implemented this formula. For the singular term an analytical formulation exists (see [26]).

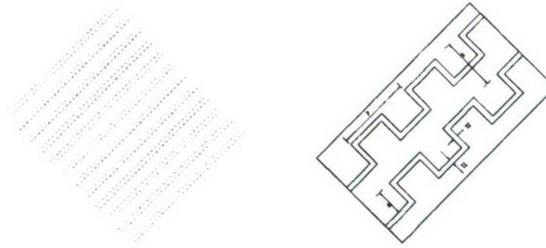


Figure 3.4 Meander-line polarizer, [27]

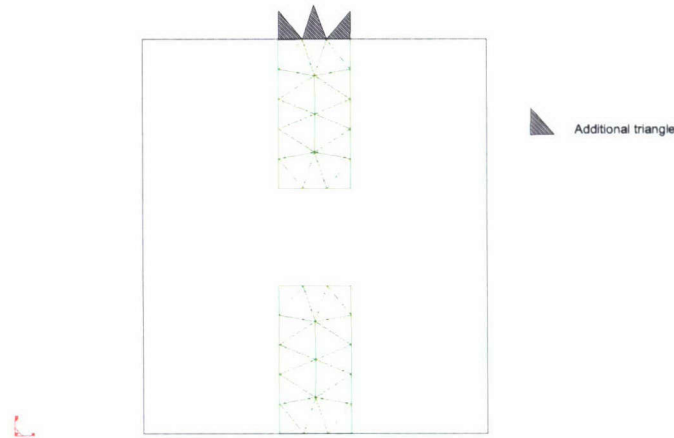


Figure 3.5 Dipole split across neighboring cells.

3.2.3 Continuity of the current

For some applications the metallic FSS element (or the aperture in the case of slot-based formulation) is continuous across adjacent unit cells. This is for example the case for polarizers, which consist of metallic grids that can be analyzed as periodically arranged simple elements, as illustrated in fig. 3.4.

In this kind of structures the current needs to be allowed to flow from a cell to the neighboring one. Independently on how we choose to mesh the structure (with triangular or rectangular elements) if we mesh only the structure inside the cell we are actually imposing equal to zero the component of the current normal to the border of the cell. To avoid this problem a simple solution consists in adding meshing elements on the borders of the cell, such that the current can flow across the border of the cell. This solution is exemplified in fig. 3.5, where the base cell of a FSS whose elements are simple dipoles is represented, and the cell has been chosen such that the dipole is split between two adjacent cells.

At present there is still a limitation when the structure is continuous in the corner of the cell, because the code is not yet able to support continuity of the current between cells with a single point in common, but only when the two cells have a common edge. This can seem a marginal problem, but it is important to deal with this kind of structures in order to exploit the so called bitmap technique, as mentioned in 2.1.2.3.

3.2.4 Results

In order to validate the new functionalities of the code TwoDim several test cases have been simulated, and the results have been compared to the results of the previous version

of the code (i.e. with rectangular mesh), and to the results obtained with the commercial software package Ansoft Designer v. 3.5. It is worth to observe that with respect to available commercial packages for electromagnetic simulation (including also Ansoft Designer), TwoDim offers many important functionalities: the modular architecture allows an efficient analysis and design of complex structures consisting of different parts (radiating elements, space/frequency filters, dielectric layers, etc) [13]; the parametrisation of the electromagnetic engine with respect to the frequency and angle of the excitation and with respect to the FSS element shapes leads to extremely short computation times for the complete characterisation of the structure at hand. From one side this accelerates the last design phase when many simulations have to be performed in correspondence of the fine tuning required prior manufacture. From the other side it represents a great base for an optimization tool, which also needs to sweep over large ranges of several parameters [30]. In commercial electromagnetic software packages, such parametrisation techniques are in general not available and optimization is a much more costly process.

3.2.4.1 Luo's array of dipoles

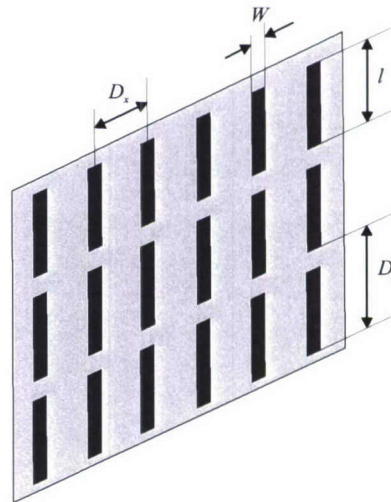


Figure 3.6 Geometry of the array of dipoles.

This is a simple single-layer FSS in free space described in [28], consisting of dipoles as FSS elements. The geometry of the array is shown in Fig. 3.6, and referring to the quantities labeled in the picture the dimensions are shown in Tab. 3.2.4.1:

| | [mm] |
|-------|-------|
| d_x | 10 |
| d_y | 10 |
| l | 7.5 |
| w | 1.875 |

Table 3.1 Dimensions for the structure represented in Fig. 3.6.

The reflection coefficient for this FSS is plotted in Fig. 3.7, together with that obtained using Ansoft Designer, and the agreements is very good.

Moreover this FSS has been simulated with the periodic grid shifted such that the dipole is split in half between two adjacent cells (as illustrated in Fig. 3.5 in 3.2.3). This

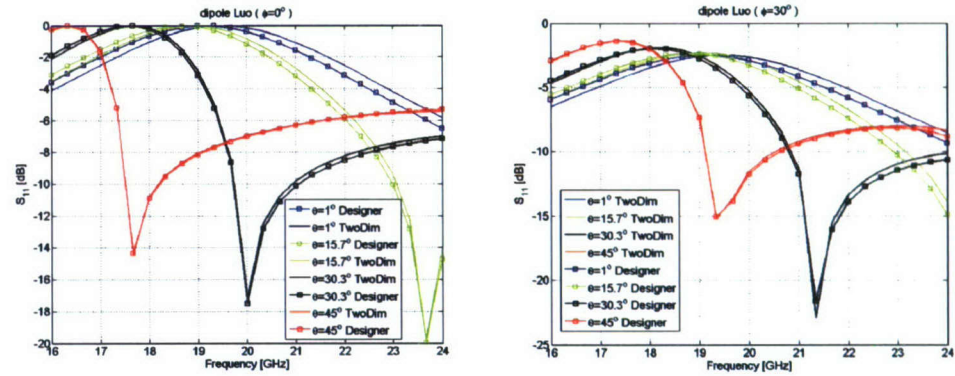


Figure 3.7 Reflection coefficient of the FSS described in Fig. 3.6.

structure has been used as a test case for the support of current continuity across the cells, and the results are shown in Fig. 3.8, for incident plane wave with $\phi = 30^\circ$.

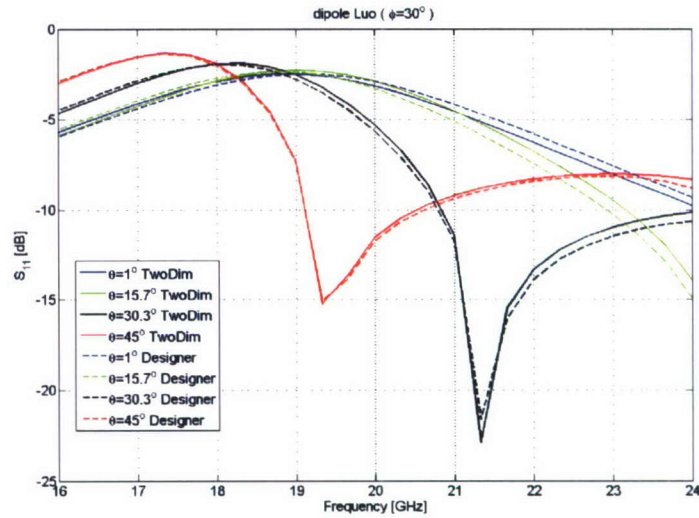


Figure 3.8 Reflection coefficient of the FSS described in Fig. 3.6 with dipoles split between adjacent cells (see 3.2.3).

3.2.4.2 Sub millimeter slots

The structure consists of three layers of equal periodic slot arrays, separated by air, and has been described in [29]. In Fig. 3.9 the geometry of the structure is represented, and the dimensions are reported in Tab. 3.2.4.2.

We compared the reflection coefficient of the structure obtained with the software Twodim with rectangular mesh to the results of Ansoft Designer. The results are illustrated in Fig. 3.10, with a plane wave impinging the FSS with $\phi = 90^\circ$ and $\theta = 45^\circ$. Also in this case the agreement is very good (the results of Twodim with rectangular mesh are omitted, but they almost overlap with the results with triangular mesh).

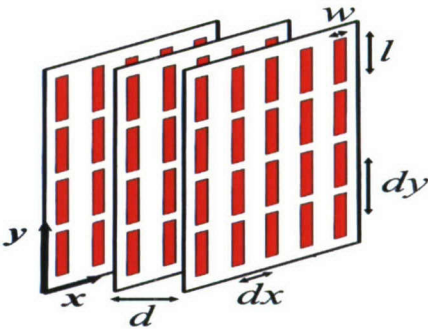


Figure 3.9 Geometry of the sub millimeter slot FSS.

| | [mm] |
|-------|-------|
| d_x | 0.49 |
| d_y | 0.5 |
| l | 0.46 |
| w | 0.015 |
| d | 0.357 |

Table 3.2 Dimensions for the structure represented in Fig. 3.9.

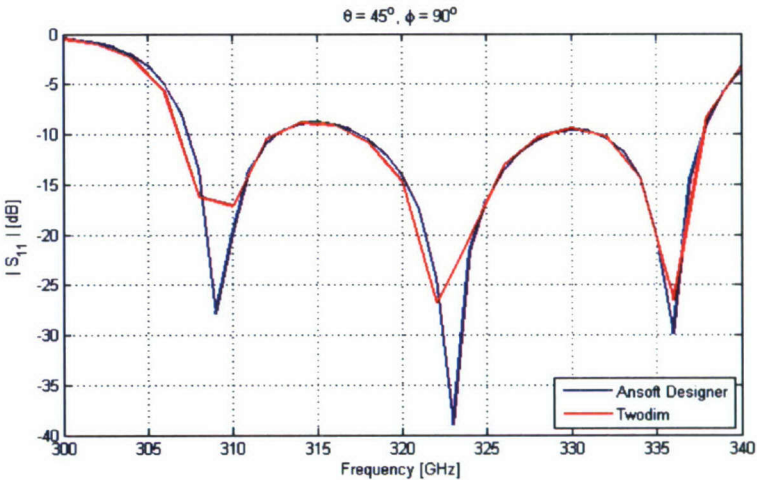


Figure 3.10 Reflection coefficient of the sub millimeter slot FSS.

3.2.4.3 *Folded dipoles*

The FSS represented in Fig. 3.11 consists of two layers of folded dipoles, in a dielectric stratification as shown in Fig. 3.12, and the relevant geometrical parameters are listed in the Tab. 3.2.4.3. The lattice is triangular, with skew angle $\Omega = 40.6^\circ$.

The reflection coefficient calculated with Twodim and with Ansoft Designer is shown in Fig. 3.13, for a plane wave impinging the FSS with $\phi = 0^\circ$ and $\phi = 30^\circ$. The agreement is good in the FSS stop band. In the pass band the difference between the two results is not significant since the level of the reflection is small (around -20 dB). Anyway it is worth to observe that. These differences however should be dependent on the IEMEN formulation, since the results obtained with Twodim and rectangular mesh (not shown in the picture) are almost overlapping the results with triangular mesh.

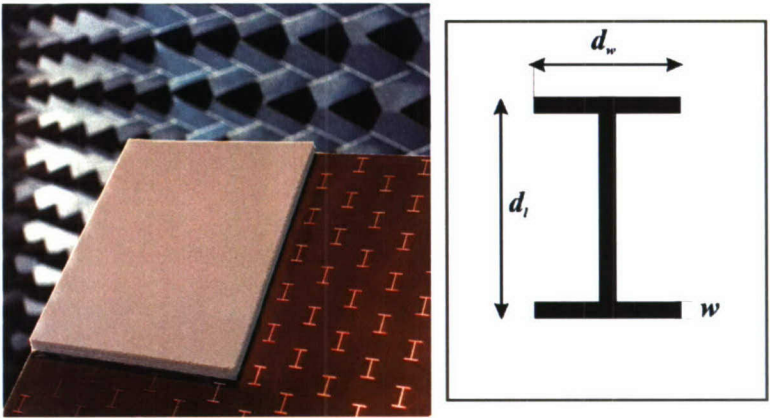


Figure 3.11 Geometry of the folded dipoles FSS.

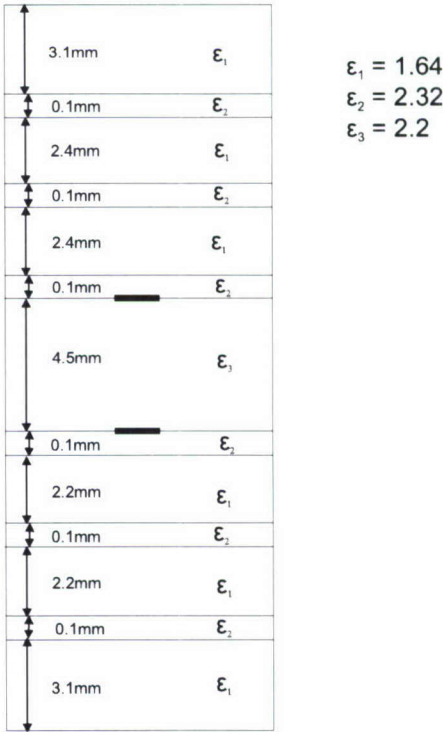


Figure 3.12 Stackup of the folded dipoles FSS.

| | |
|-------|------|
| | [mm] |
| d_w | 3.3 |
| d_l | 5.1 |
| w | 0.3 |
| D_x | 21 |
| D_y | 9 |

Table 3.3 Dimensions for the structure represented in Fig. 3.11.

3.2.4.4 Tripoles

The FSS shown in Fig. 3.14 consists of a single-layer triangular lattice of tripoles, between two layers of dielectric material with thickness equal to 0.508 mm and relative

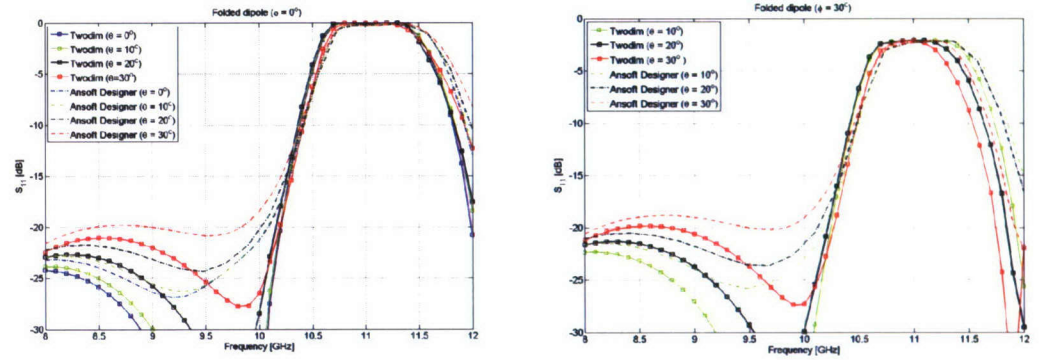


Figure 3.13 Reflection coefficient of the folded dipoles FSS.

permittivity equal to 2.2 and has been described in [7]. Referring to the picture, the dimensions are $D_x=11.934$ mm, $D_y=6.89$ mm, and skew angle equal to 30° . Each tripole (see Fig. 3.2 in Sec. 3.2.1.1) consists of three arms with length equal to 6 mm and thickness equal to 0.49 mm, with equispaced orientations (i.e. the angle between two arms of the tripole is equal to 120°).

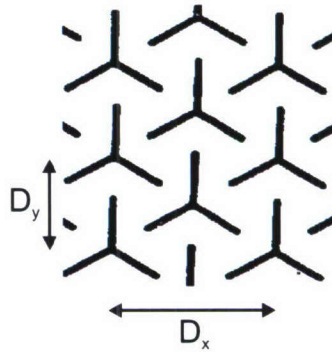


Figure 3.14 Geometry of the tripoles FSS.

This structure has been tested with oblique incidence wave excitation ($\theta = 45^\circ$), and the results are shown in Fig. 3.15. Again we can see a perfect agreement with Ansoft Designer. This is a case that can not be simulated with rectangular mesh, due to the presence of angles different than 90° .

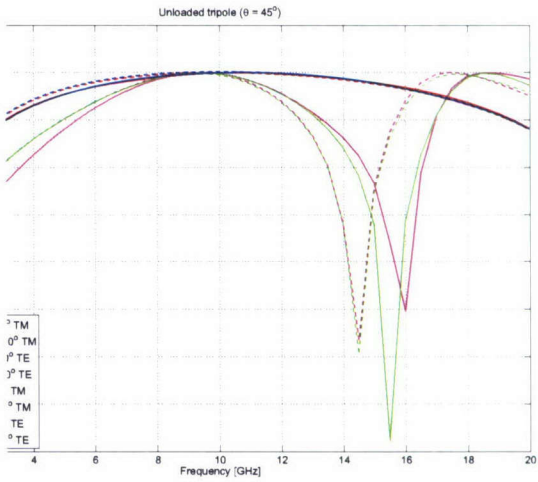


Figure 3.15 Reflection coefficient of the tripoles FSS.

4 Conclusions and Recommendations

Conclusions The activities performed in the frame of Phase I of the project on Multi-band FSSs defined within the ITM program have been aimed at the enhancement of the in-house software tool with several features needed for the analysis and design of complex FSS geometries, such as those needed for multi-band and multi-frequency structures.

In particular, the equivalent electric/magnetic current on the FSS element have been discretised using RWG basis functions, which have a triangular domain and allow the analysis of generic shapes overcoming the limitation of the originally implemented rooftop functions. Moreover, mesh refinement in certain areas of the element is now possible, while the rooftops are based on a uniform rectangular mesh and mesh refinement has to be performed on the whole FSS element resulting in a much larger number of functions (and therefore of unknowns). Correspondingly, in general a smaller number of RWGs is needed to obtain the desired result with a certain accuracy. As a consequence, analysis based on RWGs are often faster than when using rooftop functions, and lead to smaller (and better conditioned) MoM matrices. The implementation has been tested against results published in the open literature and the agreement is excellent.

Furthermore, the software tool has been extended to the analysis of FSSs whose elements are continuous across the border of the unit cell. This extension is necessary to perform a design optimization based on the bitmapping technique.

The approach proposed in this report has been successfully validated by simulating several polarizing grids with rectangular lattice. The implementation for triangular lattice grids requires further testing. Moreover, the proposed implementation is suitable when two adjacent unit cells have one metallised edge in common, but it should still be extended to the case in which a cell corner is completely metallised.

Recommendations With the new upgrades, the TwoDim software tool can be efficiently used as basis for the design of multi-band FSSs. As mentioned in the previous paragraph an aspect still needs to be investigated: the extension of the implementation for the continuity of the currents to triangular lattices and to the case of unit cells with completely metallised corners. Although this is not a fundamental limitation for the full exploitation of the bitmapping feature, we intend to tackle the problem in the first part of Phase II of the project.

5 References

- [1] T. A. Axness, R. V. Coffman, B. A. Kopp and K. W. O'Haver, "Shared Aperture Technology Development", *John Hopkins Apl. Technical Digest*, vol. 17, n. 3, 1996.
- [2] E. Walton, E. Lee, D. Kohlgraf, R. Pavlovicz, G. Bruce and B. Montgomery "Compact Shipboard Antenna System For Simultaneous Communication With Three Separate Satellites", *Ocean 2005 Conference*.
- [3] D. J. Kern, D. H. Werner, M. J. Wilhelm and K. H. Church, "Genetically engineered multiband high-impedance frequency selective surfaces", *Microwave and Optical Technology Letters*, vol. 38, n. 5, Sept. 2003.
- [4] T-K. Wu, "Four band Frequency selective Surface with Double-Square-Loop Patch Elements", *IEEE Trans. Antennas and Propag.*, vol. 42, n.12, Dec.1994.
- [5] J. Romeu and Y. Rahmat-Samii, "Fractal FSS: A Novel Dual-Band Frequency Selective Surface", *IEEE Trans. Antennas and Propag.*, vol. 48, n.7, July 2000.
- [6] R. A. Hill and B. A. Munk, "The Effect of Perturbing a Frequency Selective Surface and its Relation to the Design a Dual-band Surface", *IEEE Trans. Antennas and Propag.*, vol. 44, n.3, March 1996.
- [7] B. A. Munk, *Frequency Selective Surfaces: Theory and Design*. USA: John Wiley and Sons, 2000.
- [8] J. P. Gianvittorio, J. Romeu, S. Blanch and Y. Rahmat-Samii, "Self-Similar Prefractal Frequency Selective Surfaces for Multiband and Dual-Polarized Applications", *IEEE Trans. Antennas and Propag.*, vol. 51, n.11, Nov. 2003.
- [9] J. A. Bossard, D. H. Werner T. S. Mayer, J. A. Smith, Y. U. Tang, R. P. Drupp and L. Li, "The Design and Fabrication of Planar Multiband Metallodielectric Frequency Selective Surfaces for Infrared Applications", *IEEE Trans. Antennas and Propag.*, vol.54, n.4, April 2006.
- [10] R. P. Drupp, J. A. Bossard, D. H. Werner and T. S. Mayer, "Single Layer Multiband Infrared Metallodielectric Phtotnic Crystal designed by Genetic Algorithm Optimization", *American Institute of Physics.*, vol. 86, n.8, 2005.
- [11] TNO, Thales NL, Thales France and Ansys France, "Syntas - Synthesis Tooling for Antenna Structures, Final Report", Technical Report., November 2007.
- [12] J. M. Johnson and Y. Rahmat-Samii, "Genetic Algorithm in Engineering Electromagnetics", *IEEE Trans. Antennas and Propag. Magaz.*, vol. 39, n.4, August 1997.
- [13] S. Monni, G. Gerini, A. Neto and A.G. Tijhuis, "Multimode Equivalent Networks for the Design and Analysis of Frequency Selective Surfaces", *IEEE Trans. Antennas and Propag. Magaz.*, vol. 55, n.10, October 2007.
- [14] R. J. Bolt and T. Bertuch, "Investigation on an array configuration for multi-function radar applications", TNO Report A-212, February 2005.
- [15] S. Monni, "Frequency Selective Surfaces Integrated with Phased Array Antennas - Analysis and Design using Multimode Equivalent Networks", *PhD Thesis*, Eindhoven University of Technology, June 2005.
- [16] C. Mias, C. Tsokonas, and C. Oswald, "An investigation into the feasibility of designing frequency selective windows employing periodic structures", Technical Report, The Nottingham Trent University, Nottingham, U.K., 2002.

- [17] M. Philippakis, C. Martel, D. Kemp, M. C. S. M. R. Allan, S. Appleton, W. Damerell, C. Burton, and E. A. Parker, “*Application of FSS structures to selectively control the propagation of signals into and out of buildings*”, Technical Report, ERA Technology, Leatherhead, Surrey, U.K., 2002.
- [18] B. Widenberg and J. V. R. Rodríguez, “*Design of energy saving windows with high transmission at 900 MHz and 1800 MHz*”, Technical Report, Lund Institute of Technology, Lund, Sweden, 2002.
- [19] S. M. Hamdy and E. A. Parker, “Current distribution on the elements of a square loop frequency selective surface,” *Electronics Letters*, vol. 18, no. 14, pp. 624–624, July 1982.
- [20] N. Llombart Juan, “Development of integrated printed array antennas using EBG substrates”, Ph.D. dissertation, Departamento de Comunicaciones, Universidad Politecnica de Valencia, Valencia, Spain, 2006.
- [21] S. Rao, D. R. Wilton, A. Glisson, “Electromagnetic scattering by surfaces of arbitrary shape”, *IEEE Transactions on Antennas and Propagation*, Vol. 30, no. 3, pp. 409–418, May 1982.
- [22] V. Lancellotti, D. Milanese, R. Maggiora, G. Vecchi, V. Korytsya, “TOPICA: an accurate and efficient numerical tool for analysis and design of ICRF antennas”, *Nuclear fusion*, no. 46, pp. 476–499, June 2006.
- [23] A. H. Stroud, *Approximate Calculation of Multiple Integrals*, Englewood Cliffs, NJ: Prentice Hall, 1971.
- [24] R. D. Graglia, “On the Numerical Integration of the Linear Shape Functions Times the 3-D Green’s Function or its Gradient on a Plane Triangle”, *IEEE Transactions on Antennas and Propagation*, Vol. 41, no. 10, pp. 1448–1455, October 1993.
- [25] D. R. Wilton, S. M. Rao, A. W. Glisson, D. H. Schaubert, O. M. Al-Bundak, C. M. Butler, “Potential Integrals for Uniform and Linear Source Distributions on Polygonal and Polyhedral Domains”, *IEEE Transactions on Antennas and Propagation*, Vol. 32, no. 3, pp. 276–281, March 1984.
- [26] P. Arcioni, M. Bressan, L. Perregrini, “On the Evaluation of the Double Surface Integrals Arising in the Application of the Boundary Integral Method to 3-D Problems”, *IEEE Transactions on Microwave Theory and Techniques*, Vol. 45, no. 3, pp. 436–439, March 1997.
- [27] D. A. McNamara, “An octave bandwidth meanderline polariser consisting of five identical sheets”, *Antennas and Propagation Society International Symposium, 1981*, Vol. 19, pp. 237–240, June 1981.
- [28] X. F. Luo, A. Qmg and C. K. Leea, “The design of Frequency Selective Surfaces (FSS) Using Real-coded Genetic Algorithm (RGA)”, *Proceedings of the Fourth IEEE Pacific-Rim Conference On Multimedia*, 2003.
- [29] R. Dickie, R. Cahill, H. S. Gamble, V. F. Fusco, A. G. Schuchinsky and N. Grant, “Spatial Demultiplexing in the Submillimeter Wave Band Using Multilayer Free-Standing Frequency Selective Surfaces”, *IEEE Transactions on Antennas and Propagation*, Vol. 53, no. 6, 1904–1911, June 2005.
- [30] D.J. Bekers, S. Monni, S.M. van den Berg, A.M. van de Water, B.J. Morsink, C. Alboin, V. Ducros, M. Celikbas, J. Blanche, N. Fiscante, G. Gerini, J-P. Martinaud, M. Rochette and G.H.C. van Werkhoven, “Optimization of Phased Arrays Integrated with FSS and Feeding Elements based on Parametric Models”, *European Microwave Week 2004 Dig.*, 2004

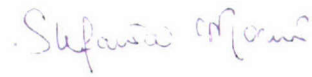
6 Signature

The Hague, August 2008

TNO Defence, Security and Safety

A handwritten signature in blue ink, appearing to read 'L.J. van Ewijk'.

L.J. van Ewijk, MSc
Head of department

A handwritten signature in blue ink, appearing to read 'Dr S. Monni'.

Dr S. Monni
Author

REPORT DOCUMENTATION PAGE
(MOD-NL)

| | | |
|---|---|---|
| 1. DEFENCE REPORT NO (MOD-NL) TD2008-0139 | 2. RECIPIENT'S ACCESSION NO - | 3. PERFORMING ORGANIZATION REPORT NO TNO-DV 2008 A325 |
| 4. PROJECT/TASK/WORK UNIT NO 032.11237 | 5. CONTRACT NO - | 6. REPORT DATE August 2008 |
| 7. NUMBER OF PAGES 39 (excl. RDP and Distribution list) | 8. NUMBER OF REFERENCES 30 | 9. TYPE OF REPORT AND DATES COVERED Final |
| 10. TITLE AND SUBTITLE Multi-band Frequency Selective Surfaces: Analysis | | |
| 11. AUTHOR(S) A. Francavilla, MSc Dr S. Monni Dr D. Bekers Dr A. Neto Dr G. Gerini N. Fiscante, MSc | | |
| 12. PERFORMING ORGANIZATION NAME(S) AND ADDRESS(ES) TNO Defence, Security and Safety, P.O. Box 96864, 2509 JG The Hague, The Netherlands Oude Waalsdorperweg 63, The Hague, The Netherlands | | |
| 13. SPONSORING AGENCY NAME(S) AND ADDRESS(ES) Ministry of Defence / Defence Materiel Organisation | | |
| 14. SUPPLEMENTARY NOTES The classification designation Ongerubriceerd is equivalent to Unclassified, Stg. Confidentieel is equivalent to Confidential and Stg. Geheim is equivalent to Secret. | | |
| 15. ABSTRACT (MAXIMUM 200 WORDS (1044 BYTE)) <p>Present trends in antenna development go toward the integration on the same antenna aperture of more functions operating in separate frequency bands. In view of this, the necessity to look at new Frequency Selective Surface (FSS) concepts becomes evident. These structures should have pass-bands corresponding to the antenna operational frequencies sandwiched between sharp stop-bands. An advanced tool has been developed at TNO for the analysis and design of multi-layer FSSs.</p> <p>In the frame of Phase I of the Multiband Frequency Selective Surface project defined within the ITM programme, the tool has been upgraded with new features that allow handling new complex geometries. The tool has been equipped with a triangular mesh and the electric and magnetic currents on the FSS elements have been discretised in terms of Rao Wilton Glisson functions. Moreover, the application of the bitmapping design technique requires considering completely metallised unit cells and therefore ensuring the continuity of the currents across adjacent cells. A further upgrade in this direction has been introduced in the tool.</p> <p>The new implementations have been tested against results available in the open literature and the obtained agreement is very good.</p> | | |
| 16. DESCRIPTORS Frequency Selective Surface Computational electromagnetics | | IDENTIFIERS Phased arrays Moment methods |
| 17a. SECURITY CLASSIFICATION (OF REPORT) Ongerubriceerd | 17b. SECURITY CLASSIFICATION (OF PAGE) Ongerubriceerd | 17c. SECURITY CLASSIFICATION (OF ABSTRACT) Ongerubriceerd |
| 18. DISTRIBUTION AVAILABILITY STATEMENT Unlimited Distribution | | 17d. SECURITY CLASSIFICATION (OF TITLES) Ongerubriceerd |

Distribution list

Onderstaande instanties/personen ontvangen een volledig exemplaar van het rapport.

- | | |
|-------|--|
| 1 | DMO/SC-DR&D standaard inclusief digitale versie bijgeleverd op cd-rom |
| 2/3 | DMO/DR&D/Kennistransfer |
| 4 | Programmabegeleider Defensie ing. L.F.Galle, DMO/DWS&B/RZS&B/OBI |
| 5 | Projectbegeleider Defensie drs. W. Pelt, DMO/DWS&B/RZS&B/OBI |
| 6 | DMO/DWS&B/RLS&B/C3I SYSN ing. E. Heertje |
| 7 | DMO/DWS&B/RZS&B/S&W LTZE1 ing. M. van Bellen |
| 8 | DMO/DWS&B/RZS&B/PLFT ir. B.R. Tjon Kam |
| 9 | DMO/DWS&B/RZS&B/PLFT ir. B.J.A.M. van Leersum |
| 10 | DMO/DWS&B/RZS&B/PLFT ir. A. de Jong |
| 11 | DMO/DWS&B/RZS&B/PLFT ing. J.M. Parent |
| 12 | DMO/DWS&B/RZS&B/MB ir. A.R. Boomstra |
| 13 | DMO/DWS&B/RZS&B/MB ing. M.M. van Gijn |
| 14 | DMO/DWS&B/RZS&B/OBI KLTZE ing. A. Kampen |
| 15 | DMO/DWS&B/RZS&B/S&W KLTZE P.F. Willemse |
| 16 | DS/DOBBP/B/MB KLTZ J. de Jonge |
| 17/19 | Bibliotheek KMA |

- 20 Programmaleider TNO Defensie en Veiligheid
 ir. Y. Rieter-Barrell
- 21/22 TNO Defensie en Veiligheid, vestiging Den Haag,
 Archief
- 23/28 TNO Defensie en Veiligheid, vestiging Den Haag,
 Business Unit Waarnemingssystemen,
 dr. ir. S. Monni
 dr. ir. D. Bekers
 dr. ir. A. Neto
 dr. ir. G. Gerini
 dr. ir. F. E. van Vliet
 ir. A. G. Huizing

The following agencies/people will receive the management summary and the distribution list of the report.

- 4 ex. DMO/SC-DR&D
- 1 ex. DMO/ressort Zeesystemen
- 1 ex. DMO/ressort Landsystemen
- 1 ex. DMO/ressort Luchtsystemen
- 2 ex. BS/DS/DOBBP/SCOB
- 1 ex. MIVD/AAR/BMT
- 1 ex. Staf CZSK
- 1 ex. Staf CLAS
- 1 ex. Staf CLSK
- 1 ex. Staf KMar
- 1 ex. TNO Defensie en Veiligheid, Algemeen Directeur,
ir. P.A.O.G. Korting
- 1 ex. TNO Defensie en Veiligheid, Directie
Directeur Operaties, ir. C. Eberwijn
- 1 ex. TNO Defensie en Veiligheid, Directie
Directeur Kennis, prof. dr. P. Werkhoven
- 1 ex. TNO Defensie en Veiligheid, Directie
Directeur Markt, G.D. Klein Baltink
- 1 ex. TNO Defensie en Veiligheid, vestiging Den Haag,
Manager Waarnemingssystemen (operaties), ir. B. Dunnebie PDeng
- 1 ex. TNO Defensie en Veiligheid, vestiging Den Haag,
Manager Informatie en Operaties (operaties), ir. P. Schulein
- 1 ex. TNO Defensie en Veiligheid, vestiging Rijswijk, daarna reserve
Manager Bescherming, Munitie en Wapens (operaties), ir. P.J.M. Elands
- 1 ex. TNO Defensie en Veiligheid, vestiging Rijswijk,
Manager BC Bescherming (operaties), ir. R.J.A. Kersten
- 1 ex. TNO Defensie en Veiligheid, vestiging Soesterberg,
Manager Human Factors (operaties), drs. H.J. Vink